



Measurement report: A survey of meteorological and cloud properties during ACTIVATE's postfrontal flights and their suitability for Lagrangian case studies

Florian Tornow^{1,2}, Ann Fridlind², George Tselioudis², Brian Cairns², Andrew Ackerman², Seethala Chellappan^{3,4}, David Painemal^{3,4}, Paquita Zuidema⁵, Christiane Voigt^{6,7}, Simon Kirschler⁶, and Armin Sorooshian⁸

¹Center for Climate Systems Research, Columbia University, New York, NY, USA

²Goddard Institute for Space Studies, NASA, New York, NY, USA

³Langley Research Center, NASA, Hampton, VA, USA

⁴Analytical Mechanics Associates, Hampton, VA, USA

⁵Department of Atmospheric Sciences, Rosenstiel School, University of Miami, Miami, FL, USA

⁶Institute of Atmospheric Physics, Deutsches Zentrum für Luft und Raumfahrt (DLR), Oberpfaffenhofen, Germany

⁷Institute of Atmospheric Physics, Johannes Gutenberg University, Mainz, Germany

⁸Department of Chemical and Environmental Engineering, University of Arizona, Tucson, AZ, USA

Correspondence: Florian Tornow (ft2544@columbia.edu)

Received: 6 November 2024 – Discussion started: 20 November 2024

Revised: 11 February 2025 – Accepted: 25 February 2025 – Published: 16 May 2025

Abstract. Postfrontal clouds, often appearing as marine cold-air outbreaks (MCAOs) along eastern seaboard, undergo overcast-to-broken cloud regime transitions. Earth system models exhibit diverse radiative biases connected to postfrontal clouds, rendering these marine boundary layer (MBL) clouds a major source of uncertainty in projected global-mean temperature. The recent NASA multi-year campaign Aerosol Cloud meTeorology Interactions oVer the western ATlantic Experiment (ACTIVATE) therefore dedicated most of its resources to sampling postfrontal MCAOs, deploying 71 flights from 2020 through 2022. We provide an overview of (1) the synoptic context within the parent extratropical cyclone, (2) the meteorological conditions with respect to the season, (3) the suitability of case data and measurements for Lagrangian analysis and modeling studies, and (4) the encountered cloud properties. A proposed subset of flights deemed most suitable for Lagrangian modeling case studies is highlighted throughout. Such flights typically cover a greater fetch range, were better aligned with the MBL wind direction, and revisited sampled air masses when key instruments were operational. Like many other flights, these flights often probed cloud formation and some cloud regime transitions. Surveying cloud properties from remote sensing and in situ probes, we find a great range in cloud-top heights and a relatively large concentration of frozen hydrometeors, which suggest strong free tropospheric entrainment and secondary ice formation, respectively. Both processes are expected to leave marked signatures in cloud evolution, such as strongly ranging cloud droplet number concentrations. ACTIVATE data combined with satellite retrievals can establish observational constraints for future model improvement work.

1 Introduction

Postfrontal low-level clouds occur frequently over the extratropical oceans globally. Their relatively poor representation in earth system models (ESMs; e.g., Bodas-Salcedo et al., 2014) and undetermined cloud–climate feedback (e.g., Frey and Kay, 2018; McCoy et al., 2019; Zelinka et al., 2022; McCoy et al., 2023) substantially contribute to the uncertainty in global-mean temperature projections (Bock et al., 2020; Zelinka et al., 2020). Thus, postfrontal clouds emerge as an important target for field campaigns and subsequent model–observation intercomparison to test and improve ESMs. Efforts to improve ESM cloud physics have often benefited from side-by-side comparison of large-eddy simulations and ESM simulations in single-column model (SCM) mode (e.g., Neggers, 2015). The SCM simulations efficiently express parent ESM column physics skill and bias while being forced by well-defined boundary conditions, which typically reflect synoptic conditions leading to problematic cloud representation, hereafter referred to as modeling case studies. Where horizontal advection is large (e.g., in postfrontal situations), these boundary conditions can be extracted along Lagrangian trajectories that follow the cloudy air mass, thereby enabling simulations of a horizontally translating domain that are locally free of leading horizontal advective tendencies (e.g., Neggers, 2015; Pithan et al., 2019).

Postfrontal clouds, often appearing as marine cold-air outbreaks (MCAOs), are challenging to represent in ESMs (Pithan et al., 2019). After the cold front of an extratropical cyclone passes continental eastern coastlines, including the US eastern seaboard, a north-westerly flow of stronger wind speed typically sets in, transporting relatively cold air over a relatively warm ocean surface and spurring intense turbulent surface fluxes (e.g., Painemal et al., 2023). The subsiding motion in the free troposphere (FT) aloft, often associated with dry intrusions (Browning, 1997; Raveh-Rubin, 2017), creates a capping inversion under which marine boundary layer (MBL) clouds begin forming at some distance downwind of the coastline. In MCAOs, these initial MBL clouds often appear as cloud streets (Brümmer, 1999). After filling in towards a nearly or fully overcast cloud deck within the MBL farther downwind, clouds then transition towards a broken, sometimes open-cellular deck at greater fetch. There is evidence that the different morphologies (i.e., overcast versus broken clouds) coincide with distinct meteorological boundary conditions (McCoy et al., 2017; Chen et al., 2022). A key driver of the cloud regime transitions is often the formation of substantial precipitation (e.g., Abel et al., 2017; Tornow et al., 2023; Seethala et al., 2024; Kirschler et al., 2023). Hydrometeor collisions, leading to coalescence of droplets, droplet collection by rain drops, and droplet collection by frozen hydrometeors (riming), efficiently reduce the number concentration of cloud droplets and thereby aerosol available as cloud condensation nuclei and thereby the number concentration of cloud droplets. Below-cloud scavenging of

aerosol can further remove cloud condensation nuclei. Similar to drizzle-driven transitions in the subtropics (Yamaguchi et al., 2017), the loss of cloud condensation nuclei amplifies subsequent precipitation formation, creating a positive feedback loop that is especially efficient where cloud condensate reaches high mixing ratios (Wood et al., 2017). With intensifying precipitation, sub-cloud evaporation of precipitation progressively stratifies the MBL, inhibiting vertical transport of heat, moisture, and cloud condensation nuclei (often referred to as decoupling; e.g., Abel et al., 2017; Yamaguchi et al., 2017), thereby transforming a stratiform-natured cloud deck into a convective-natured one (Field et al., 2014; Tomassini et al., 2017) and presenting challenges for ESM physics in representing the coupled microphysical and dynamical processes (Pithan et al., 2019).

Aircraft and surface-based campaigns provide crucial measurements to improve our understanding of regional MCAO cloud regimes. For example, GALE (Genesis of Atlantic Lows Experiment, Dirks et al., 1988) probed extratropical cyclones and MCAO clouds over the north-west Atlantic. NAAMES (North Atlantic Aerosols and Marine Ecosystems Study, Behrenfeld et al., 2019) probed MCAOs farther north, illuminating ocean and meteorological processes modifying size and mass composition with fetch (e.g., Sanchez et al., 2018). A more comprehensive overview for the NW Atlantic is provided by Sorooshian et al. (2020). Much farther downwind, the ACE-ENA (Aerosol and Cloud Experiments in the Eastern North Atlantic, Wang et al., 2019) campaign sampled sporadic postfrontal passages, often after cloud regime transitions had occurred. Over the Norwegian Sea, COMBLE (Cold-Air Outbreaks in the Marine Boundary Layer Experiment, Geerts et al., 2022) similarly sampled MCAOs from a surface site ~ 1000 km downwind of MCAO inception and connected to an upwind site near inception (e.g., Williams et al., 2024), enabling a model–observation intercomparison focused on aerosol–cloud interactions in sub-Arctic MCAOs (Juliano et al., 2024). Additional MCAO data over the Norwegian Sea have now been gathered during the recent CAESAR (Cold-Air Outbreak Experiment in the Sub-Arctic Region) campaign. A comprehensive set of field campaigns focused on MCAO in northern latitudes, including flight campaigns with bases in Spitsbergen, Norway, and Kiruna, Sweden, for example, (AC)³ (Wendisch et al., 2023) that included AFLUX (Aircraft campaign observing FLUXes of energy and momentum in the cloudy boundary layer over polar sea ice and ocean), MOSAiC-ACA (Multidisciplinary Drifting Observatory for the Study of Arctic Climate – Airborne observations in the Central Arctic, Mech et al., 2022; Moser et al., 2023), and HALO-(AC)³ (High-Altitude and Long-Range Research Aircraft – (AC)³ project, Wendisch et al., 2024).

This study focuses on postfrontal MCAO flights during the recently concluded multi-year NASA Earth Venture Sub-orbital (EVS) campaign ACTIVATE (Aerosol Cloud meteorology Interactions oVer the western ATLantic Experi-

ment, Sorooshian et al., 2019). ACTIVATE deployed two aircraft that flew in tandem most of the time (Schlosser et al., 2024) and carried advanced instrumentation (Sorooshian et al., 2023): (1) a high-flying King Air equipped with remote sensing instruments and dropsondes and (2) a low-flying Falcon that porpoised through the MBL and FT, comprehensively measuring aerosol and cloud properties using in situ probes. The base of operations for almost all ACTIVATE flights was the NASA Langley Research Center (LaRC) in Hampton, Virginia, with flights typically being 3–4 h with a subset of days with more desirable conditions having two tandem flights on the same day. Between the years 2020 and 2022, a total of 162 joint flights took place (Sorooshian et al., 2023), of which 71 flights show maximum marine cold-air outbreak indices (here defined as $M = \theta_{\text{srf}} - \theta_{850 \text{ hPa}}$) greater than zero and are further examined here. An advantage of the multi-year deployment is the ability to perform repeated measurements during a specific season over multiple years, thereby building substantial statistics of key properties. To date, a few selected MCAOs have been targeted, but a comprehensive overview has not been done. Li et al. (2021) examined 28 February and 1 March 2020 using Eulerian LES (large-eddy simulation) and explored the dependence on meteorological forcing. With a focus on 1 March 2020, Chen et al. (2022) investigated the mesoscale cloud morphology in mesoscale simulations, while Tornow et al. (2022) studied aerosol dilution from FT entrainment. Seethala et al. (2024) surveyed numerous flights (i.e., 1 March 2020, 29 January 2021, 3 February 2021, 5 March 2021, and 8 March 2021) to explore mixed-phase cloud microphysical properties with distance from the coast.

This paper aims to provide (1) an overview of the synoptic conditions and the associated meteorological properties during ACTIVATE's postfrontal flights; (2) an assessment of the eligibility of each flight to align well enough with the prevalent wind direction and cover a wide enough fetch range, among others, to support a Lagrangian analysis or modeling case study; and (3) a survey of encountered cloud properties. We propose a subset of flights as most suitable for Lagrangian case studies and survey that subset compared with all flights and the postfrontal class as a whole. The paper is organized as follows: Sect. 2 describes the data and methodology, Sect. 3 contains the overview analysis, Sect. 4 discusses the results, and Sect. 5 provides conclusions.

2 Data and methods

2.1 Identification of cold front and low-pressure center locations

To identify cold front locations, we apply two techniques and thereby broadly follow earlier studies (e.g., Naud et al., 2016) in (1) searching for strong spatial features in potential temperature fields (Hewson, 1998) and (2) searching for strong temporal changes in wind speed and direction (Simmonds et

al., 2012). We explain both methods in more detail below. For meteorological fields, we rely on the MERRA-2 reanalysis (Gelaro et al., 2017), which has been extensively compared to ACTIVATE data (Seethala et al., 2021). A resulting frontal location can be seen in Fig. 1. We note that MERRA-2 and other reanalyses are expected to locate widespread and long-lived mid-latitude postfrontal sectors quite accurately spatiotemporally. However, we consider MERRA-2 to less reliably predict quantities such as liquid and ice water path and associated cloud cover and albedo (Pithan et al., 2019). This motivates the use of reanalysis fields to contextualize ACTIVATE aircraft data for improving the understanding of MCAO microphysics and radiative impacts.

First, we use MERRA-2 potential temperature at 850 hPa, θ , and spatially smooth fields by computing a moving-window average using a 3×3 grid window (translating into a $1.5^\circ \times 1.875^\circ$ latitude–longitude box) and then calculate spatial derivatives following Hewson (1998) and updates provided in Berry et al. (2011): a first-order derivative ($\frac{d\theta}{d[x/y]}$) signifying temperature change in longitudinal as well as latitudinal direction and second- and third-order derivatives of absolute temperature changes ($\frac{d}{dx}|\frac{d\theta}{dx}|$ and $\frac{d^2}{dx^2}|\frac{d\theta}{dx}|$). In addition, we compute the along-wind divergence using MERRA-2 850 hPa horizontal winds, \mathbf{v}_h , and above-second-order derivatives ($\mathbf{v}_h \frac{d}{dx}|\frac{d\theta}{dx}|$). After excluding points within temperature dips (i.e., in areas where first-order and second-order derivatives align in sign) and where the product of first-order and normalized second-order derivatives are small (excluding values above a threshold of $0.5 \times 10^{-10} \text{ K m}^{-1}$), we select points near third-order derivatives that are zero (i.e., extreme thermal gradients) and apply a threshold to filter for small along-wind divergence (values below 0.75 m s^{-1}). Lastly, we connect filtered points towards lines by looping over all points and searching within 250 km for neighboring members. Lines that exceed a maximum member-to-member distance of 250 km are considered fronts. Where available, we filter for line length greater than 500 and 1000 km.

Second, following Simmonds et al. (2012), we extract MERRA-2 fields at time steps 3 h before and after the time of interest. We filter for grid points of strong 850 hPa meridional wind speed changes ($\frac{d|v_h|}{dt} > 1/3 \text{ m s}^{-1} \text{ h}^{-1}$) and change in meridional wind direction (a switch in sign of the v_h component). Again, we connect filtered points by lines by looping over all points and searching within 250 km for neighboring members.

Lastly, we locate the low-pressure center as a simple minimum in surface pressure, limiting ourselves to the NW Atlantic domain (lat $< 55^\circ \text{ N}$ and long $< -40^\circ \text{ E}$).

2.2 Lagrangian trajectories

We construct underlying MBL Lagrangian trajectories at every 10 min along each track flown by the Falcon aircraft. Using MERRA-2 three-dimensional wind fields (inst3_3d_asm_Nv) at the time step closest to the time of in-

Identification of Storm Features during ACTIVATE case 2022-03-29

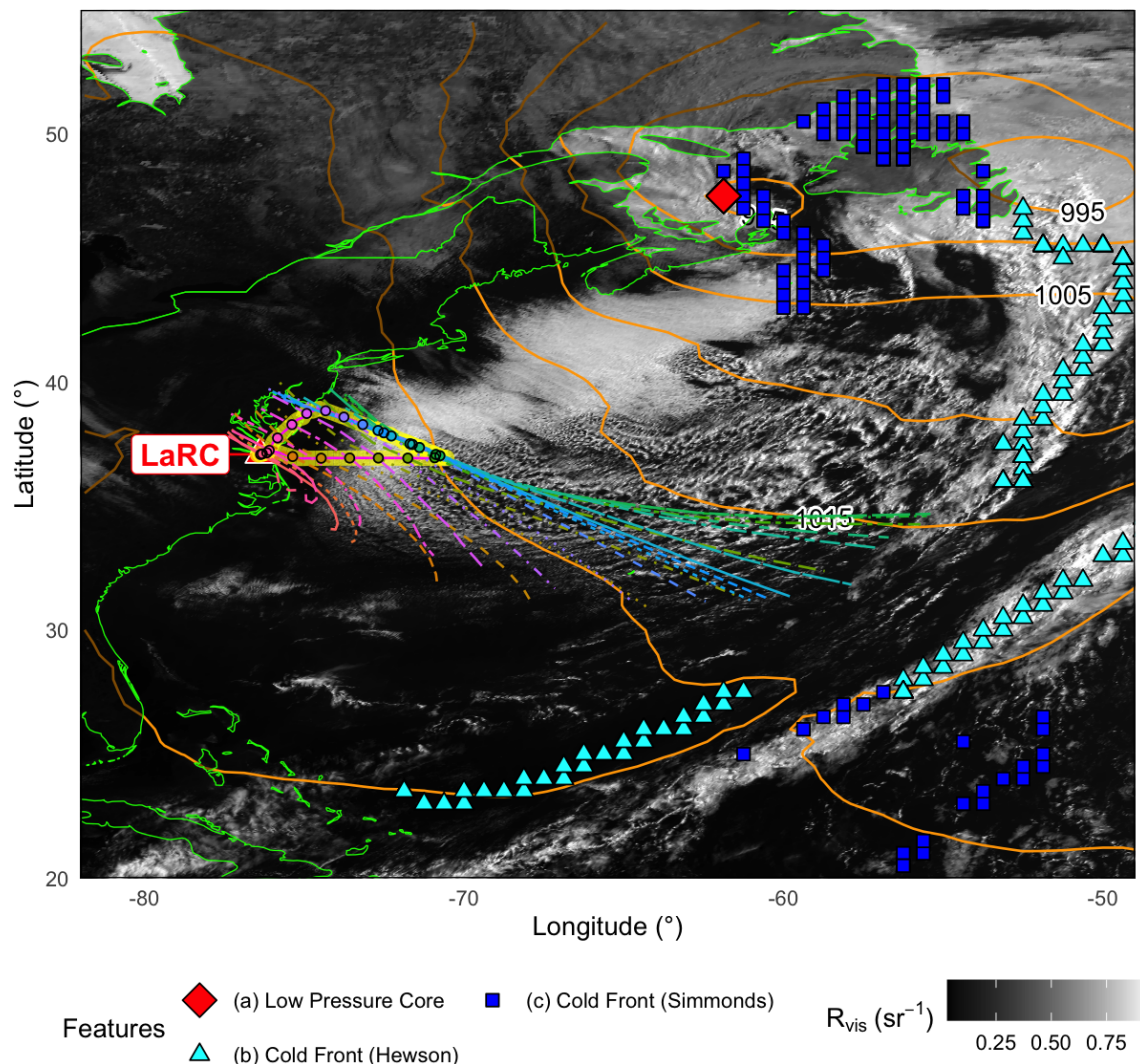


Figure 1. For a marine cold-air outbreak during the second flight on 29 March 2022, we demonstrate the identification of the low-pressure center (red diamond) as well as cold front locations using two approaches (cyan and blue symbols; Sect. 2.1). Along the flight track (yellow line), we launch Lagrangian back and forward trajectories every 10 min (dots along track and lines of same color), clipped to only cover ocean surfaces (country borders shown in green lines). The background shows coinciding GOES-16 visible imagery (black–white scale) and MERRA-2 surface pressure (orange lines) corresponding to the midpoint of the flight time. The red–white triangle labeled with LaRC marks the air base in Hampton, Virginia.

terest, we interpolate horizontal wind components at a given start location and an altitude of 250 m, which we assume is representative of the MBL (e.g., Seethala et al., 2021). Using these winds, we then compute the expected position at the next time step (i.e., after 3 h) and iterate the above procedure for 30 h into the future and also 15 h into the past, totaling a 48 h trajectory. Along each trajectory, we collocate MERRA-2 surface pressure; sea-surface temperature (SST); sensible and latent heat fluxes; and profiles of horizontal and large-scale vertical wind, relative humidity, and water vapor and cloud condensate mixing ratios. We use SST to limit trajectories to portions over the ocean.

2.3 GOES-16 SatCORPS retrieval

To each of the MBL Lagrangian trajectories we collocate GOES-16 cloud retrievals that are typically available every 20 min. We approximate the location along the trajectory by interpolating latitude and longitude at acquisition time. We collect cloud retrievals within a window of ± 50 km in the cross-track and ± 25 km in the along-track direction, effectively forming a wind-oriented box of 100×50 km².

Cloud optical depth (COD) is retrieved during the day- and nighttime. Daytime COD is primarily derived from the 0.64 μm channel, whereas nighttime COD (solar zenith an-

gle $> 82.5^\circ$) is estimated from three infrared channels (Minnis and Heck, 2012). The nighttime physical algorithm is only sensitive to clouds with COD < 6.0 , and for those clouds, the retrievals compare well against independent observations (Minnis and Heck, 2012). For COD > 6.0 , the algorithm is unable to discern the exact COD magnitude, and thus, these values should only be used for qualitative purposes (e.g., identification of optically thick clouds). Lastly, we determine cloud cover within the box by computing the portion of pixels with COD > 2.5 (Wyant et al., 1997). Retrievals are provided at a $4 \text{ km} \times 4 \text{ km}$ resolution at nadir. While including clouds of all heights, we verify that clouds are mostly of low-level character (see Sect. 2.5). Figure A1 shows $\sim 75\%$ of cloud-top heights within 3.5 km of the surface and $\sim 15\%$ above 5.0 km.

2.4 Selected ACTIVATE remote sensing and in situ measurements

In addition to the flight track (i.e., using the Falcon aircraft location and timestamp unless stated otherwise), we collect measurements from selected remote sensing instruments and in situ probes aboard the King Air and the Falcon, respectively.

- SPEC Fast Cloud Droplet Probe (FCDP, Knop et al., 2021; Kirschler et al., 2022) measures aerosol and cloud particles in the diameter size range of 3–50 μm , sorted into 18 size bins, and reports N_d as sum of all bins as well as the particle number concentration in each bin.
- SPEC 2D Stereo Probe (2D-S, Lawson et al., 2006; Kirschler et al., 2023) covers hydrometeors in the diameter size range of 11.4–1465 μm sorted into 128 size bins. Particle size distributions are derived from FCDP for particles $< 30 \mu\text{m}$ and from 2D-S for particles $> 30 \mu\text{m}$, and particles $< 100 \mu\text{m}$ are assumed to be liquid droplets as no other information was available (Kirschler et al., 2023). Hydrometeors greater than 100 μm are classified into the liquid or frozen ice phase by the shape of the 2D-S image and reported as the sum of all frozen hydrometeors N_i . The classification algorithm conservatively labeled hydrometeors as liquid when imagery was ambiguous, leading to a small number ($< 1\%$) of false positives for frozen hydrometeors but sporadically elevated ($< 40\%$) false positives for liquid hydrometeors.
- Condensation particle counters TSI CPC-3776 and CPC-3772 measured condensation nucleus (CN) concentrations greater than 3 and 10 nm, respectively.
- Research Scanning Polarimeter (RSP, Cairns et al., 1999) performed passive polarimetric cloud remote sensing when Sun–object–observer geometries were such that scattering angles from $135\text{--}155^\circ$, where the

cloud bow is located, were observable. The location and structure of the cloud bow provides detailed information about the cloud-top droplet size distribution. During winter and spring deployments, this meant that the angle between the aircraft heading and the bearing of the Sun had to be between 10 and 20° .

- High-Spectral-Resolution Lidar 2 (HSRL-2, Burton et al., 2018) performed active temperature, aerosol, and cloud remote sensing whenever located over ocean, measuring backscatter signals at 355 and 1064 nm, allowing, among others, to retrieve cloud-top height and cloud-top temperature, the latter obtained from vertical temperature profiles at the altitude of the former.

King Air measurements were collocated to Falcon ones via their nearest timestamp. In most cases, the aircraft were distanced less than 6 km and within 5 min (Schlosser et al., 2024). The reader is referred to Sorooshian et al. (2023) for more details about the instrumentation and flight strategy details.

2.5 Evaluation criteria to assess combined case and flight qualities

Per ACTIVATE flight, we verify a range of criteria (listed in Table 1 and also shown in Fig. 4, left). Criteria are derived from ACTIVATE in situ and remote sensing data, Lagrangian trajectories, and collocated GOES-16 cloud cover. These criteria are designed to indicate several qualities:

1. The first criterion is stereotypical postfrontal conditions that often emerge as MCAOs. We filter for an eastward boundary layer wind direction (primarily eastward flow) that is expected from extratropical cyclone dynamics in the postfrontal sector (e.g., Tselioudis and Grise, 2020). To obtain strong MCAOs that are expected to undergo faster cloud regime transitions in better reach of the aircraft during ACTIVATE, we also impose a MCAO index threshold (maximum MCAO index $> 10 \text{ K}$), which we also consider a proxy for elevated surface fluxes (and were therefore left out as a criterion). Typically prevalent large-scale subsidence should disallow high-level clouds that may hinder satellite retrievals; we examine GOES-16 retrievals to verify the absence of high-level clouds (high cloud fraction $< 10\%$).
2. The second criterion is flights that followed the MBL air mass in a quasi-Lagrangian and also Lagrangian manner, with key instruments being operational. We use trajectory and flight path locations to measure spatial alignment, rewarding alignment during a sizable fraction of the flight (downwind portion with respect to flight $> 20\%$) and additionally over a certain distance (downwind distance $> 200 \text{ km}$) that we consider large enough to detect cloud property changes. We fur-

ther examine if RSP, a key instrument used to measure cloud micro- and macrophysical properties, was able to probe a sizable portion (“Downwind RSP availability > 30 %”) across this distance. Lastly, we explore the availability of Lagrangian air mass revisits, ensuring that horizontal legs are long enough to have aircraft probes collect data (minimum duration of Lagrangian legs > 1 min). We apply a similar metric to RSP as well (“Lagrangian RSP availability”) to ascertain favorable potential Sun–object–observer geometries.

3. The final criterion is, where possible, liquid and frozen precipitation-sized hydrometeors that may drive the larger cloud regime transitions and elevated aerosol concentrations from new particle formation that may delay transitions. We use data from in situ cloud probes to indicate the presence of the various hydrometeor types (frozen hydrometeors measured, drizzle-sized particles measured, and rain-sized particles measured). We additionally survey in situ aerosol probes for traces of new particle formation; we use condensation nucleus ratios to indicate the presence of freshly nucleated particles $3 \text{ nm} < D_p < 10 \text{ nm}$ (recent particle formation frequency > 5 %; e.g., Corral et al., 2022) that are expected to grow to larger sizes and drastically increased concentrations (high aerosol concentration frequency > 5 %).

The criteria can be readily modified in the archived code base but are currently set to verify at least a few times across all flights. For example, selecting a radius exceeding 20 km for downwind portion with respect to flight > 20 % would increase the chance for this criterion to verify, while increasing the fetch range in downwind distance > 200 km would diminish chances.

3 Results

3.1 Large-scale cyclonic context

From all ACTIVATE tandem flights coinciding with positive MCAO indices, we first locate features of the parent extratropical cyclone that allow us to put flight data into a larger meteorological context. From coinciding MERRA-2 meteorological fields, we identify the low-pressure center and the cold front location. Figure 1 shows an example from 29 March 2022 via satellite imagery and meteorological fields closest to the morning flight (thick yellow line). The two frontal identification methods (Sect. 2.1) are somewhat complementary and line up with frontal clouds in geostationary imagery:

1. Searching for spatial gradients in temperature and wind fields and connecting clusters of strong gradients (Hewson, 1998) typically finds areas of greater baroclinicity and results here in elongated structures farther away from the low.

2. Searching for grid boxes that experienced above-threshold temporal changes in wind speed and direction (Simmonds et al., 2012) and connecting greater clusters typically locates areas of smaller baroclinicity, resulting in regions near the low-pressure center.

Uncertainties are expected where MERRA-2's 3 h resolution fails to resolve fast-translating portions of the front, for example, between -72 and -60°E (i.e., at the bottom of the Fig. 1), that is identified as farther west and disconnected from its north-eastern extension, contrary to satellite imagery.

Figure 2 summarizes all flights by their surface pressure differences to the nearest identified cold front (x axis) and the low-pressure center (y axis), with positive differences typically indicating a position to the west of the cold front and to the south of the low, respectively. ACTIVATE flights cover a broad range within postfrontal areas, in particular where pressure differences between flight portion and cold front and the low fall between 0 and 20 hPa as well as 10–60 hPa, respectively. In a few instances, the ACTIVATE flights reached the cold front (i.e., a pressure difference to cold front smaller 0 hPa). Color shading in Fig. 2 panels shows reanalysis-based MBL horizontal and FT large-scale vertical wind speed of all flight points. Both panels reveal a general tendency for increased MBL wind speed and more positive vertical motion (with few incidents of lofting motion) closer to the low and the front, broadly matching earlier extratropical cyclone composites from satellite imagery (Field and Wood, 2007; Naud et al., 2016) and in line with the general schematic of a heterogeneously subsiding dry intrusion (Browning, 1997).

3.2 Comparison to seasonal meteorology

ACTIVATE targeted postfrontal conditions, thereby avoiding other meteorological regimes (e.g., frontal passage with vertically extended clouds or regimes dominated by high surface pressure). To put the meteorological properties during flights into a greater seasonal context, we extracted MERRA-2 fields averaged over the campaign domain (i.e., a triangle spanning 32.50°N , 80.00°W ; 32.50°N , 65.00°W ; and 40.50°N , 72.25°W). For the season from November 2021 through March 2022, Fig. 3 shows timelines for selected meteorological parameters and their histogram (shown as box-whisker plots on the far right). In addition to the overall season and dates during postfrontal ACTIVATE flights, we also show a proposed subset of flights that may provide valuable Lagrangian case studies for analyses and modeling work, as analyzed in greater detail in Sect. 3.3. Figure 1 depicts one of the flights within this subset.

As best seen in the timeline of surface fluxes (Fig. 3d), postfrontal conditions occurred regularly, as often as every 3–4 d (e.g., in January 2022), and ACTIVATE probed about a third of all events. Compared to the greater season over the campaign domain (blue), ACTIVATE flights (grey) gen-

Table 1. Criteria to indicate specific qualities of each postfrontal flight and its synoptic condition represented through Lagrangian trajectories.

Statement	Data and methodology
Primarily eastward flow	Uses Lagrangian trajectories and checks whether most meridional wind components are positive within the first 12 h
Maximum MCAO index > 10 K	Uses Lagrangian trajectories and computes the median across all trajectories' maximum MCAO = $\theta_{\text{srf}} - \theta_{850\text{hPa}}$
High cloud fraction < 10 %	Uses Lagrangian trajectories and checks whether collocated GOES-16 cloud properties contain show fewer than 10 % of data points with a cloud-top height above 5 km
Downwind portion with respect to flight > 20 %	Uses flight track coordinates and Lagrangian trajectories to first determine the portion of the track falling within 20 km of each trajectory and then report whether any portion is greater than 20 %
Downwind distance > 200 km	For extent of alignment (see above, aligning more than 20 % of the track with a trajectory), checks whether the downwind distance along the flight track exceeds 200 km
Downwind RSP availability > 30 %	For long downwind distances (see above, a distance greater than 200 km for cases of great alignment), checks whether RSP is available for more than 30 % of the time
Minimum duration of Lagrangian legs > 1 min	From all portions of the flight track falling within 20 km and 10 min of a trajectory, quantifies the number of samples taken at up- and downwind portions, and reports whether the minimum duration covers at least 1 min
Lagrangian span > 1.5 h	From all portions of the flight track falling within 20 km and 10 min of a trajectory, measures the greatest time span across samples
Lagrangian RSP availability	From all portions of the King Air track, measured whether RSP is available during at least 100 acquisitions (i.e., totaling about 1.5 min of data) at up- and downwind portions
Frozen hydrometeors measured	Checks whether 2D-S reported any particles classified as frozen hydrometeors
Drizzle-sized particles measured	From FCDP and 2D-S size distributions of liquid particles, determines whether the count of particles with diameter greater than 40 μm is above zero (note that particles smaller than 108 nm are all assumed liquid; Sect. 2.4)
Rain-sized particles measured	From 2D-S size distributions of liquid particles, determines whether the count of liquid particles with diameter greater than 100 μm is above zero
Recent particle formation frequency > 5 %	Determines the portion of the flight track that shows a $\text{CN}_{3\text{nm}}/\text{CN}_{10\text{nm}}$ ratio greater 1.8 (e.g., Corral et al., 2022; Namdari et al., 2024) and reports whether the threshold is exceeded more than 5 % of the time
High aerosol concentration frequency > 5 %	Determines the portion of the flight track that shows a $\text{CN}_{10\text{nm}}$ greater than 10 000 cm^{-3} and reports whether the threshold is exceeded more than 5 % of the time

erally coincided with greater subsiding motion, roughly similar wind speeds, and considerably greater MCAO indices that also resulted in considerably larger surface fluxes. The subset of flights with most Lagrangian sampling during ideal postfrontal conditions (red) tends to represent relatively strong MCAOs, as evidenced by interquartile range (IQR) values above the IQR of all postfrontal flights as well as the overall season (shown from top to bottom in Fig. 3): vertical motion is more negative (median of -25.0 mm s^{-1} compared to -8.4 and -1.0 mm s^{-1} for all flights and the overall season, respectively), wind speed is greater (median of 10.6 m s^{-1} compared to 6.6 and 8.2 m s^{-1} , respectively), and MCAO indices (median of 7.4 K compared to 3.0 and -1.8 K , respectively) and resulting turbulent surface fluxes are greater (median of 550 W m^{-2} compared to 300 and 190 W m^{-2} , respectively), where latter is expected to increase with near-

surface wind speed and surface-air differential in temperature and humidity. The above example season is representative of ACTIVATE's earlier off-summer deployments in spring 2020 and fall 2020 through spring 2021, which are shown in Fig. A2. Note that sample size is smaller in Fig. A2, preventing box-whisker plots from reliably producing whiskers.

3.3 Potential for case studies

To utilize the ACTIVATE field observations for Lagrangian LES and SCM simulations, flights ideally must have captured

1. eastward flow associated with typical postfrontal synoptic conditions free of high-level clouds, for example, seen via the trajectories in Fig. 1;

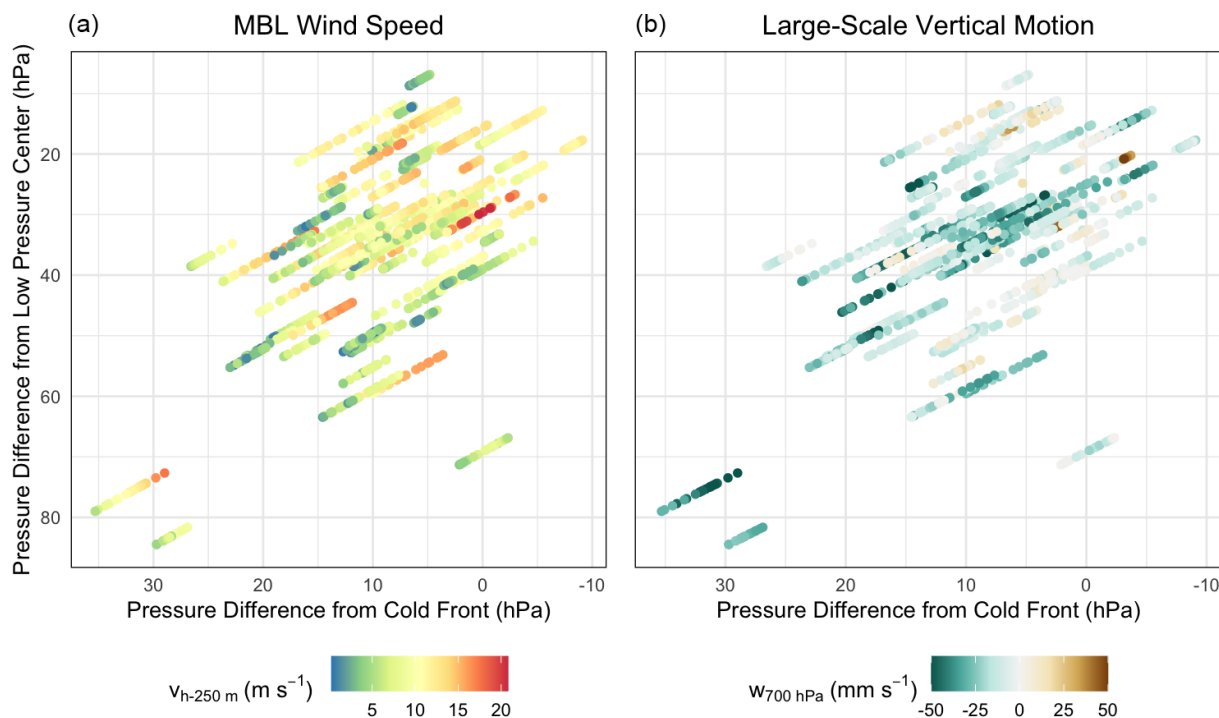


Figure 2. For all ACTIVATE tandem flights during postfrontal conditions, we measure the smallest pressure difference to cold front (x axis) and low-pressure center (y axis). Panels (a) and (b) show the same data points but different shadings: 250 m horizontal wind speed (a) and large-scale vertical motion at 700 hPa (b), where 700 hPa is expected to represent free tropospheric conditions.

2. relatively large MCAO indices associated with well-defined cold-air outbreak conditions;
3. MBL flow along near-parallel Lagrangian trajectories to effectively capture the downwind evolution of the boundary layer flow; and
4. sufficient fetch to sample MBL evolution (i.e., sufficient distance to detect process signatures, such as cloud condensation nucleus decrease from precipitation formation) and with key instruments operating (e.g., RSP being the most volatile one owing to limited Sun–object–observer geometries for operation), in the best scenario probing an air mass more than once to establish a true Lagrangian sample (i.e., free of stationarity assumptions).

Additionally, we indicate whether flights capture

5. both warm and cold precipitation particles, which are expected to affect cloud regime transition when appearing in substantial concentrations;
6. recent new particle formation that undergoes particle growth and could result in aerosol particles large enough to act as cloud condensation nuclei (Zheng et al., 2021; Tornow et al., 2025), in particular during enhanced updraft speeds, where more particles are activated (e.g., Kirschler et al., 2022).

These criteria are defined in greater detail in Sect. 2.5. Figure 4 (left) presents a score sheet, verifying criteria for all postfrontal flights. All flights fulfill at least three scores, for example, 2 March 2020 (RF015) only providing eastward flow and warm precipitation-type hydrometeors while 26 January 2022 leg 1 (RF111) only provided all three precipitation-type hydrometeors (i.e., drizzle, rain, and frozen hydrometeors) and good alignment between flight and trajectory, leaving all other criteria unchecked. About two-thirds of the flights present an eastward flow, about half have high MCAO indices, and about half are free of high clouds. Four out of five flights attributed a large portion (i.e., more than 20 %) of their resources aligned with a Lagrangian trajectory, but only two out of five captured a large enough fetch (i.e., more than 200 km), and about half had RSP data available for much of the downwind portion (i.e., more than 30 %). While air mass revisits are nearly unavoidable on mostly non-linear flight tracks, two out of five flights did so with horizontal legs long enough (i.e., at least 1 min) to gather measurements from all instruments or even obtain a statistic based on a small amount of data. In about two-thirds of all flights, the revisit happened after a significant amount of time (i.e., at least 1.5 h), and one in five flights had RSP observations available when revisiting. All flights captured warm-phase precipitation hydrometeors, but only about two-thirds of all flights collected frozen hydrometeors, in many instances aligning with an unchecked MCAO index criterion.

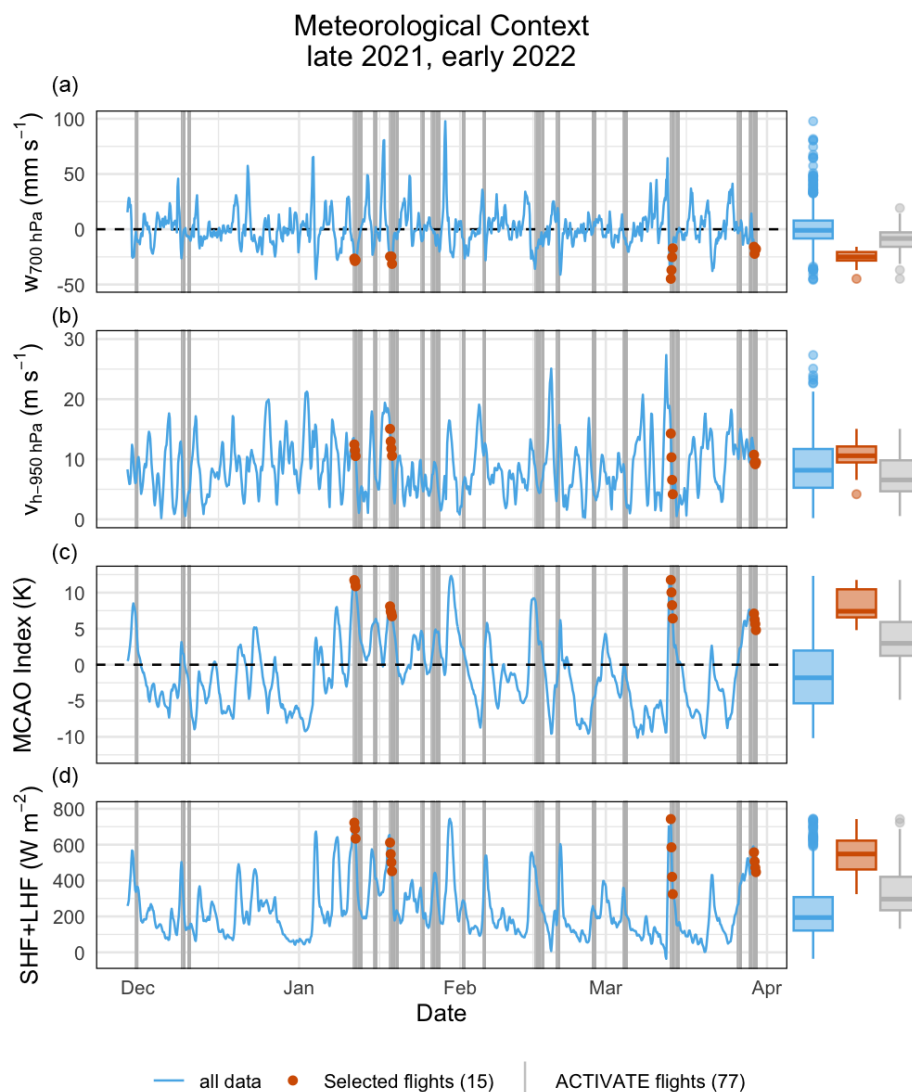


Figure 3. Averaged over the ACTIVATE domain and during the period of 29 November 2021 until 30 March 2022, we extract 3 h meteorological parameters from MERRA-2 (from top to bottom): **(a)** large-scale vertical motion at 700 hPa; **(b)** horizontal wind speed at 950 hPa; **(c)** MCAO index, defined as $\text{MCAO} = \theta_{\text{srf}} - \theta_{850\text{hPa}}$; and **(d)** lumped turbulent surface fluxes. Compared to the complete time series (blue lines), ACTIVATE flights (gray vertical bars) targeted specific conditions and selected flights (red dots) form a particular subset. Box-whisker plots (right) mark the overall distribution of all three groups. The legend also lists the number of data points used for box-whisker plots.

About half the flights show signs of new particle formation and about a third measured elevated aerosol concentrations during non-negligible portions of the flight (i.e., more than 5 % of a flight saw concentrations greater than $10\,000\text{ cm}^{-3}$).

Selected flights (marked through a red outline in the score sheet) show generally a greater score. For example, the pair of flights on 29 March 2022 (RF147 and RF148) fulfills all required criteria, rendering it a particularly strong case for Lagrangian modeling and analysis. The pair of flights on 1 March 2020 (RF013 and RF014) fulfills nearly all criteria, only lacking RSP along quasi-Lagrangian stretches during the first flight and elevated MCAO indices during the second one. The combination of the two flights is still expected to

produce excellent case data by, for example, relying on up-wind data from the first flight and downwind data from the second one. The single flight on 3 February 2021 (RF044) checks all but one required criterion that should still produce excellent case data: the relatively short cloud regime transition was captured by the flight (Fig. A3) but resulted in a quasi-Lagrangian stretch shorter than 200 km. The single flight on 29 January 2021 (RF042) lacks two Lagrangian aspects, including long enough horizontal legs and RSP being available. The flights on 13 March 2022 (RF137 and RF138) lack RSP during Lagrangian air mass revisits, and the first flight covers a quasi-Lagrangian stretch shorter than 200 km. The pair of flights on 11 January 2022 (RF100 and RF101)

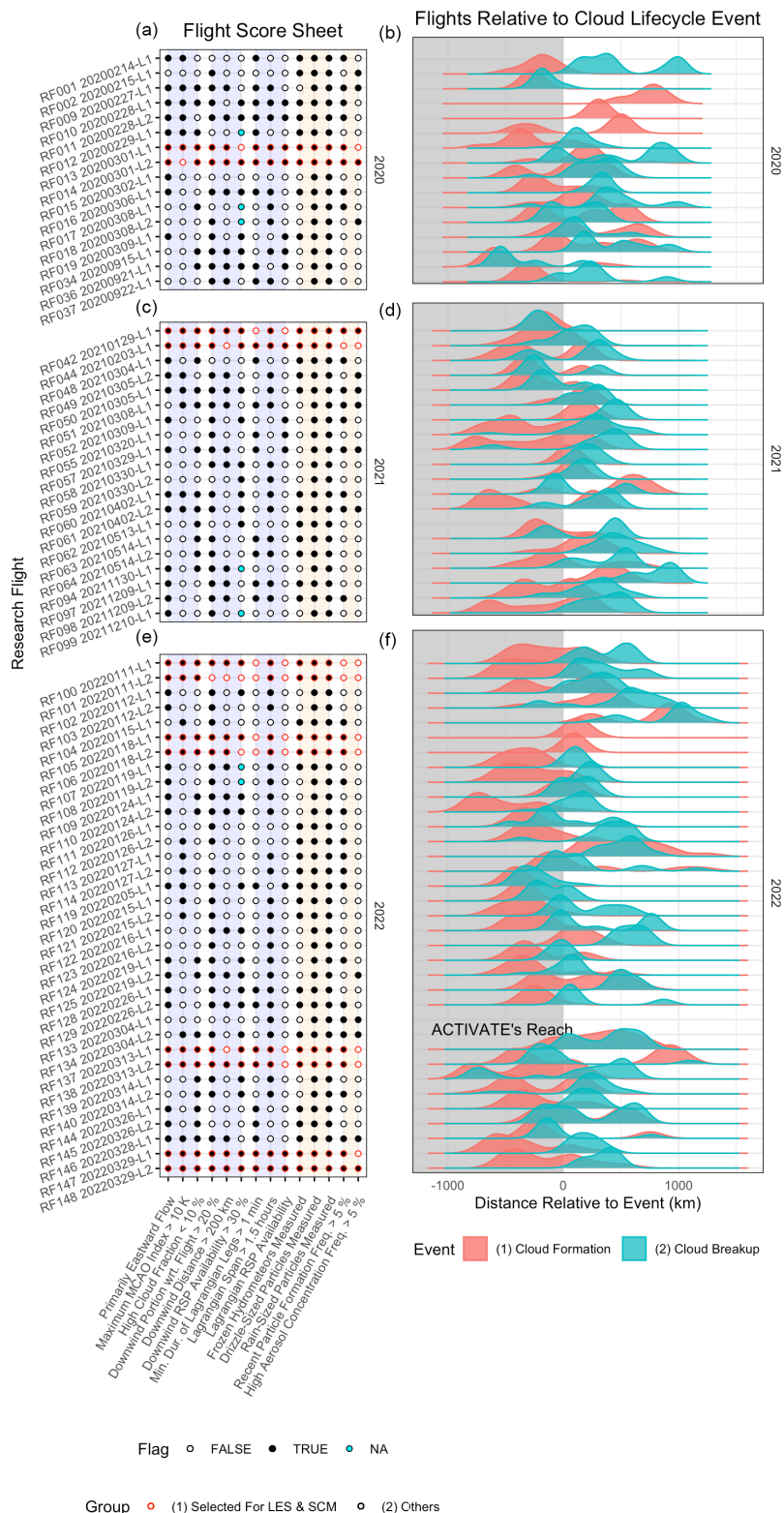


Figure 4. For all tandem flights under postfrontal conditions, we summarize the veracity of criteria in a score sheet (a, explained in greater detail in Sect. 2.5 and grouped into categories marked by shaded areas with blue and orange marking criteria of primary and secondary importance, respectively) and display the relative distance of flight data compared to cloud formation and breakup (b, gray areas mark fetch values reached by ACTIVATE, explained in greater detail in Sect. 3.3). L values next to dates (YYYYMMDD format) correspond to the launch number (e.g., L1 is the first flight – i.e., launch – of that given day).

satisfies most criteria during the first flight, with the expectation of prolonged Lagrangian revisits and with RSP being available, while the second flight lacks all quasi-Lagrangian aspects. The pair of flights on 18 January 2022 (RF105 and RF106) only lacks RSP availability during the quasi-Lagrangian stretch of the second flight, and Lagrangian sampling aspects in both flights. All selected flights show both liquid and frozen hydrometeor particles being present. Only a few flights show elevated aerosol particle counts, for example, the second flight on 1 March 2020 (RF014), the single flight on 29 January 2021 (RF042), and the second flight on 29 March 2022 (RF148), while indication of new particle formation is present in most flights, with the exception of 3 February 2021 (RF044) and 11 January 2022 (RF100 and RF101).

Complementary to the score sheet, we summarize which portion of the greater cloud life cycle was probed. Ideally, flights captured both cloud formation as well as the cloud regime transition to a broken state farther downwind. Figure 1 provides an example where the aircraft first passed the cloud-free area off the eastern seaboard and then the formed cloud deck, including its brightest location, and lastly accessed the dimmer, broken cloud field farthest east before turning around.

To quantify this exposure to different stages, we perform the following steps. Per Lagrangian trajectories (launched every 10 min along each flight track), we collocate GOES-16-based cloud cover (Sect. 2.3), available every 20 min. From the resulting timeline of cloud cover, we then extract two events:

1. cloud formation, defined as the first instance exceeding a cloud cover of 75 %, and
2. cloud breakup, defined as the first instance of cloud cover below 75 % after formation.

Figure A4 provides an example for all trajectories during the second flight on 29 March 2022 (RF148). Per cloud life cycle event, we then calculate its timing and distance to the flight (i.e., the trajectory launch).

Figure 4 (right) shows the distribution of distances using all trajectories. Negative values (also highlighted by gray shading as well as ACTIVATE's reach) mean that ACTIVATE aircraft were located downwind of an event (e.g., in clouds that increased beyond 75 % past cloud formation), likely passing the event on its way out, whereas positive values (white shading) mean that an event was located farther downwind than seen by aircraft (e.g., in clouds that have yet to increase towards 75 % cloud cover for cloud formation). The above ideally translates into both events – cloud formation (red) and cloud breakup (cyan) – being inside the negative range. Most flights only probed the formation of clouds (i.e., red values are in the negative range) and left their regime transition unobserved (i.e., cyan values are in the positive range). For example, Fig. 1's flight on 29 March 2022

(RF148) just reached the breakup stage, similar to the other selected flights. Where trajectories intercepted a cloud deck that was too thin or too broken (to exceed a cloud fraction of 75 %), such as on 22 September 2020 (RF037), no red or cyan curves are shown.

In a few instances, flights probed both stages robustly. Seen in combination with the score sheet, these flights, however, lack other qualities. For example, on 30 November 2021 (RF094) and 10 December 2021 (RF099), RSP was unavailable, and there was no Lagrangian element. In general, few flights are of a high score and also show proximity to both life cycle events, such as the second flight on 28 February 2020 (RF011), which, however, displayed an atypical cloud cover evolution, likely due to uncommon upward motion (Li et al., 2021) in connection with an apparent smaller front (Fig. A3).

3.4 Cloud properties during flights

Next, we survey cloud properties seen by ACTIVATE that enable us, for example, to develop an expectation for prevalent microphysical processes (e.g., mixed-phase processes like riming) as discussed in Sect. 4. We collect cloud macrophysical retrievals from HSRL-2 remote sensing (cloud-top height and temperature) and microphysical properties measured by FCDP and 2D-S in situ probes (cloud droplet number and frozen hydrometeor concentrations) as explained in greater detail in Sect. 2.4.

Figure 5 summarizes each property through three percentiles, 5th, 50th, and 95th, per flight. Across all cases, clouds generally occupy the lower 2.5 km of the atmosphere, in a few instances extending to 3.5 km (e.g., 30 November 2021, RF094), which typically translates into cloud-top temperatures between -10 and $+5$ °C with a few instances of smaller and greater temperatures. All cases span a wide range of cloud droplet number concentrations, with median values between 100 and 500 cm^{-3} , while extremes (here 95th percentiles) can exceed values of 1500 cm^{-3} in rare cases, for example, on 24 January 2022 (RF109 and RF110) as well as on 8 and 9 March 2021 (RF051 and RF052, respectively). Most frozen hydrometeor concentrations show median values around 1 L^{-1} , but extremes can reach concentrations that are 2 orders of magnitude higher, such as on 28 February 2020 (RF010 and RF011).

The selected subset (shown in red) shows relatively typical cloud-top heights (median values ranging between 1500 and 2100 m) but colder cloud-top temperatures (median values between -12 and -5 °C). Droplet number concentrations show relatively typical median values (between 200 and 500 cm^{-3}) but can extend beyond 1000 cm^{-3} in their extremes (e.g., 1 March 2020, RF013 and RF014, and 29 March 2022, RF147 and RF148). The selected cases show frozen hydrometeor concentrations within the overall range.

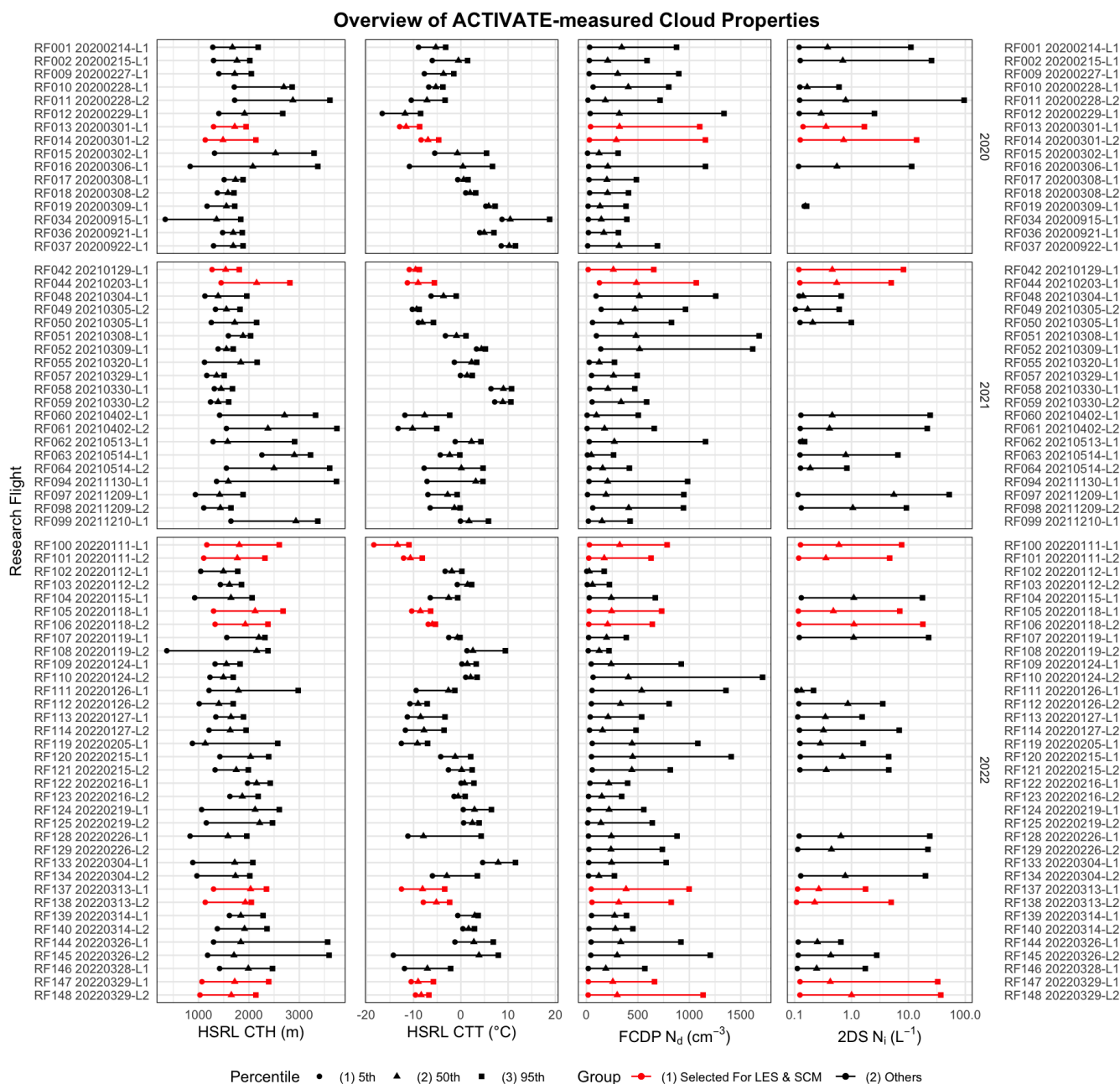


Figure 5. Using each flight's in situ and remote sensing data, we summarize various cloud properties (from left to right): cloud-top height (CTH), cloud-top temperature (CTT), cloud droplet number concentration (N_d), and frozen hydrometeor number concentration (N_f). Percentiles (symbols) indicate the distribution, with horizontal lines spanning 5th and 95th percentiles. Note that the x axis of the rightmost panel is shown in logarithmic scale. Selected cases are shown in red.

3.5 Evolution of selected cases

Lastly, we examine the cloud macrophysical and meteorological evolution of the selected cases. Drawing from GOES-16 cloud cover along trajectories (e.g., seen in Fig. A5), we compute time with respect to their surface flux maximum. As shown in Fig. 6a, we find a uniform cloud cover increase across all cases, with overcast conditions reaching around

0 h for all cases, except on 1 March 2020. Thereafter, cloud cover decreases as part of the cloud regime transition and reaches a broad range of levels, ranging anywhere between 30 % and 80 %, bracketed by 1 March 2020 and 13 March 2022 on the low and high end, respectively. The selected days also display a diverse evolution in cloud-top temperature (Fig. 6b), roughly matching the range probed by ACTIVATE remote sensing (Fig. 5) near 0 h. MERRA2-based

MCAO indices along trajectories (Fig. 6c) show a collective decrease after the maximum, with cases retaining their relative strength (e.g., 11 January 2022 remains strongest throughout). MERRA2-based large-scale subsidence shows vastly different values with strong fluctuations over time but always displays negative median values (i.e., downward motion, Fig. 6d).

In summary, we find ACTIVATE to have successfully sampled postfrontal conditions, probing a broad range of locations within postfrontal sectors. These conditions, naturally, deviate from synoptic conditions across the overall season. A few cold-air outbreak flights that tend to deviate more strongly in their meteorology show qualities that are desirable for Lagrangian LES and SCM cases: they cover a sizable portion of a typical boundary flow, capturing cloud formation and at least brief portions of the cloud regime transition to the broken state via key remote sensing and in situ instruments. Cloud properties show sizable differences across those flights, with selected flights typically at the lower end of cloud-top temperature but all other properties within the pack.

4 Discussion

The cloud properties seen in Fig. 5 lend themselves to speculate about dominant processes. For example, a great range in cloud-top height could result from substantial MBL deepening with fetch. Deepening against FT subsidence translates into substantial entrainment at the MBL top, mixing in FT air that typically shows a lower concentration of aerosol available as cloud condensation nuclei and thereby dilutes MBL concentrations (Tornow et al., 2022). As an example among the selected flights, 1 March 2020 shows a spread of about 1000 m in cloud-top height and was assessed to have a peak entrainment rate of 12 cm s^{-1} . Other selected flights also largely line up with the boundary flow and cover similar ranges in cloud-top height, except for 11 January 2022, which shows about 1500 m. Second, the presence of large frozen hydrometeor concentrations and the prevalent range in cloud-top temperatures imply secondary ice processes at play. The date 28 February 2020 shows up to $N_i \leq 100 \text{ L}^{-1}$, reaching, like many other flights, cloud-top temperatures of -13 to -4 °C (i.e., 5th and 95th percentiles) that may be favorable to ice multiplication processes that are considered highly uncertain (e.g., Fridlind and Ackerman, 2018; Korolev et al., 2020; Korolev and Leisner, 2020; Seidel et al., 2024). Frozen hydrometeors have often shown signs of riming during ACTIVATE (Seethala et al., 2024), which may in turn impact the cloud regime transition (Tornow et al., 2021).

The selected cases constitute generally strong MCAOs and should provide excellent targets for weather and climate model development. While ACTIVATE covers a wider spectrum of conditions, the selected subset forms a robust statistical sample of unique mixed-phase clouds. The range in

meteorological forcing and resulting cloud cover and cloud-top temperature evolution provides a test bed for model developers to explore the inclusion of uncertain mixed-phase processes and benchmark against a comprehensive set of observational targets from ACTIVATE and satellite. The wide range in cloud-top temperature has the potential to serve as proxy for a warming climate and assess cloud–climate feedback.

The criteria utilized in Sect. 3 may provide a blueprint for future deployments. Building on the growing experience of setting up Lagrangian case studies for LES and SCM in the community, the list of criteria would likely be refined or extended. For ACTIVATE, the air base at LaRC was conveniently located upwind of postfrontal clouds, thereby allowing for automatically sampling initial upwind conditions needed for case studies, while the more challenging part was reaching downwind locations. Therefore, many criteria target the latter challenge. For aircraft campaigns that are located at the downwind portion, additional criteria may be required, for example, the ability to gather upwind conditions.

Where flights fall short of capturing cloud regime transitions, the use of satellite data can be helpful. As done in pre-campaign (Tornow et al., 2023) and campaign efforts (Tornow et al., 2025), low-Earth orbiting as well as geostationary satellite retrievals may provide observational constraints. Among the most valuable constraints are instantaneous total liquid water path retrievals from microwave radiometers aboard a fleet of low-Earth orbiting satellites (Elsaesser et al., 2017), complementing aircraft retrievals of liquid water path where available (e.g., Ephraim et al., 2024), and cloud cover, obtained from day–night COD retrievals using geostationary imagery (used here to identify life cycle stages).

5 Conclusions

Our analysis of ACTIVATE's tandem flights during postfrontal conditions supports the following conclusions:

1. Aircraft data covered a wide range of locations within postfrontal sectors and represent typical MBL horizontal and FT vertical wind speeds.
2. The dedication to postfrontal clouds facilitated distinct meteorological conditions that exceed the seasonally typical conditions of FT subsidence, MCAO indices, and resulting turbulent surface fluxes. A proposed subset of cold-air outbreak flights that are well suited to Lagrangian analyses constitutes even greater MBL wind speed, FT subsidence, MCAO indices, and surface fluxes compared to all postfrontal flights. The selected flight days include 1 March 2020, 29 January 2021, 3 February 2021, 11 and 18 January 2022, and 13 and 29 March 2022.

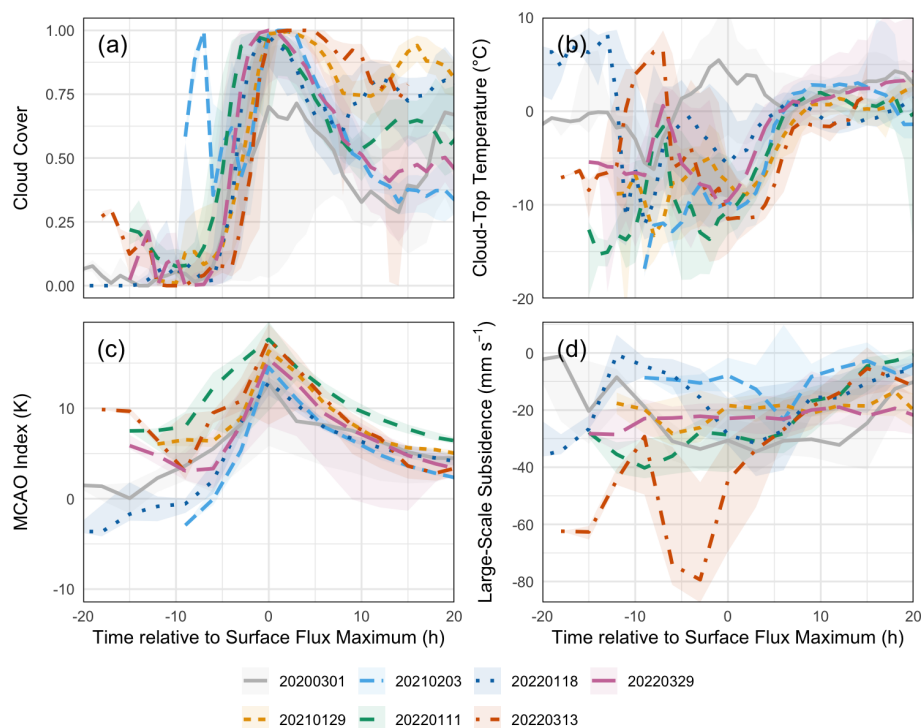


Figure 6. Relative to each trajectory's time of surface flux maximum, we present statistics (i.e., median shown as lines and interquartile range shown as shading) per selected case, showing GOES-16 cloud properties and MERRA-2 meteorological boundary conditions: (a) cloud cover, (b) cloud-top temperature, (c) MCAO index, and (d) $w_{700\text{hPa}}$.

- Criteria that aim to measure the ability of flight data to serve in Lagrangian LES and SCM case studies reveal a wide range of qualities. The selected flights typically cover a large fetch in MBL flow direction, have key instruments operating, and often exhibit evidence of specific aerosol and cloud processes. These flights experience the formation of clouds but typically have only briefly visited the cloud regime transition towards a broken cloud deck. The use of satellite retrievals offers a way to obtain observational constraints farther downwind.
- Remote sensing and in situ probes reveal a wide range of cloud macro- and microphysical properties that suggest the presence of dominant processes, such as strong FT entrainment, riming, and secondary ice formation.

ACTIVATE data provide a unique resource to study cloud controlling processes in MCAOs and improve the representation of clouds and aerosol in upcoming ESM improvement work.

Appendix A: Supporting figures

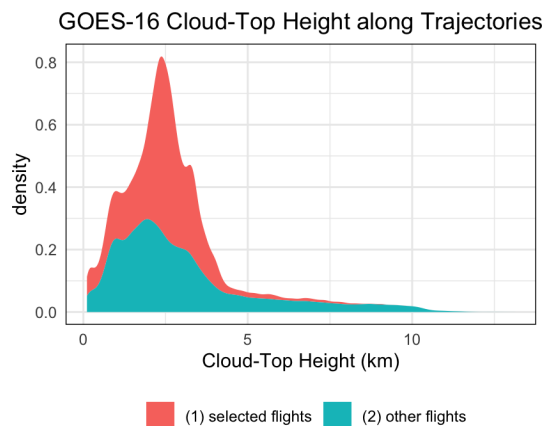


Figure A1. From GOES-16 cloud-top heights that we collocated along all trajectories, we produce stacked density functions for two categories.

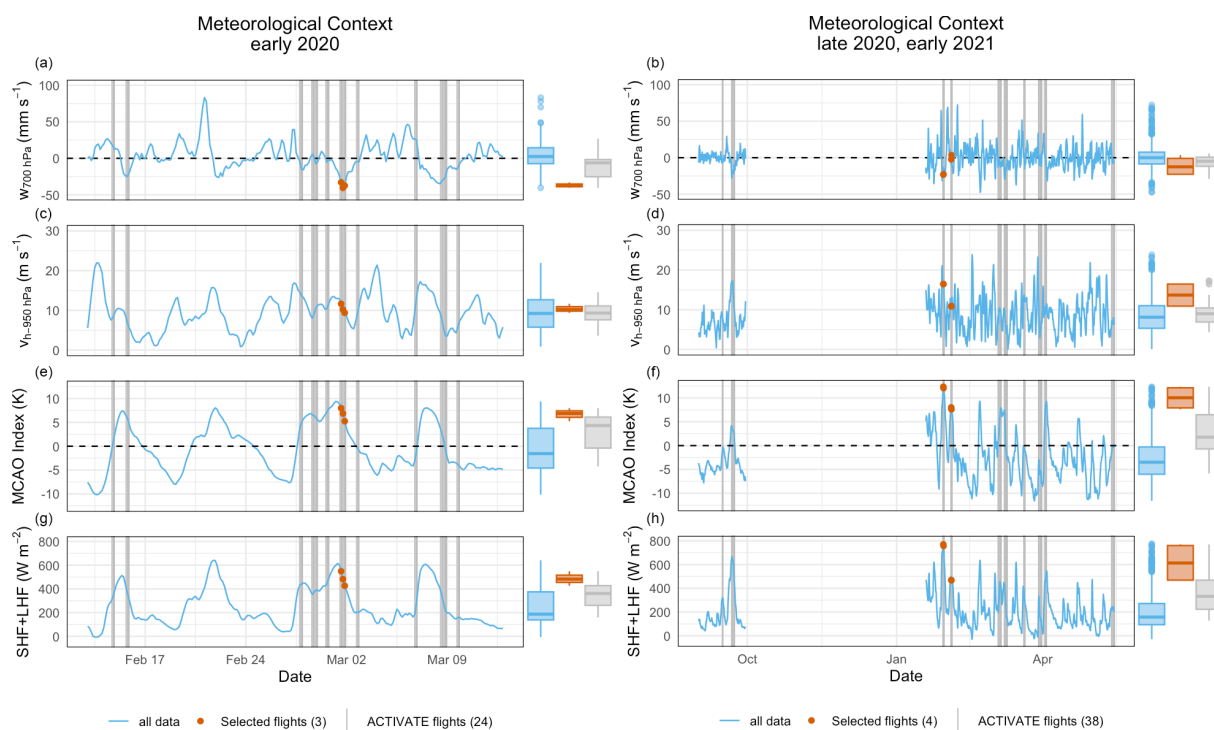


Figure A2. Like Fig. 3, here shown for the two earlier deployments. Note that both panels contains too few data points in the selected flights category to produce whiskers.

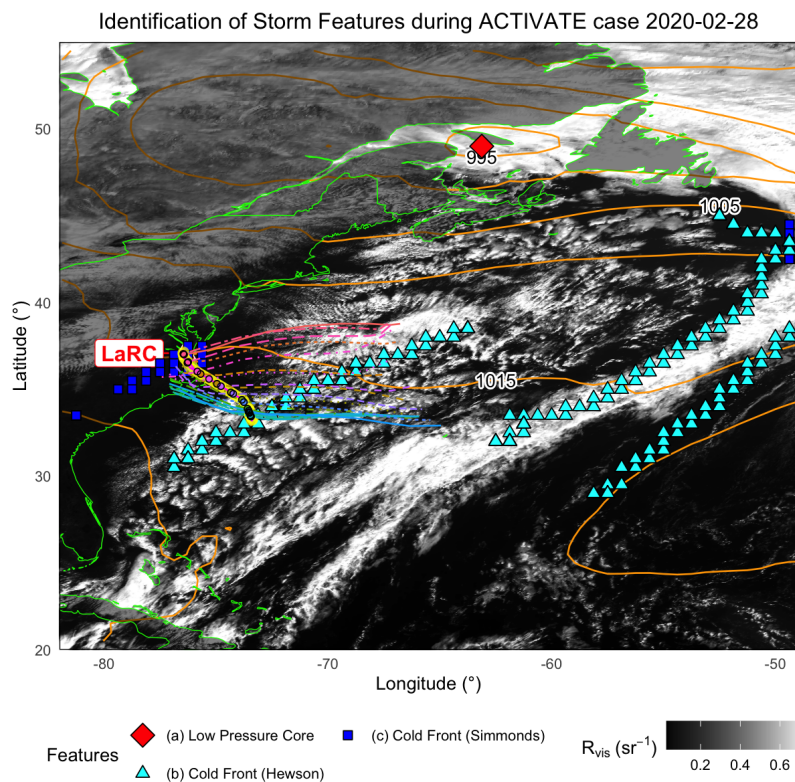


Figure A3. Similarly to Fig. 1, we present data for 28 February 2020.

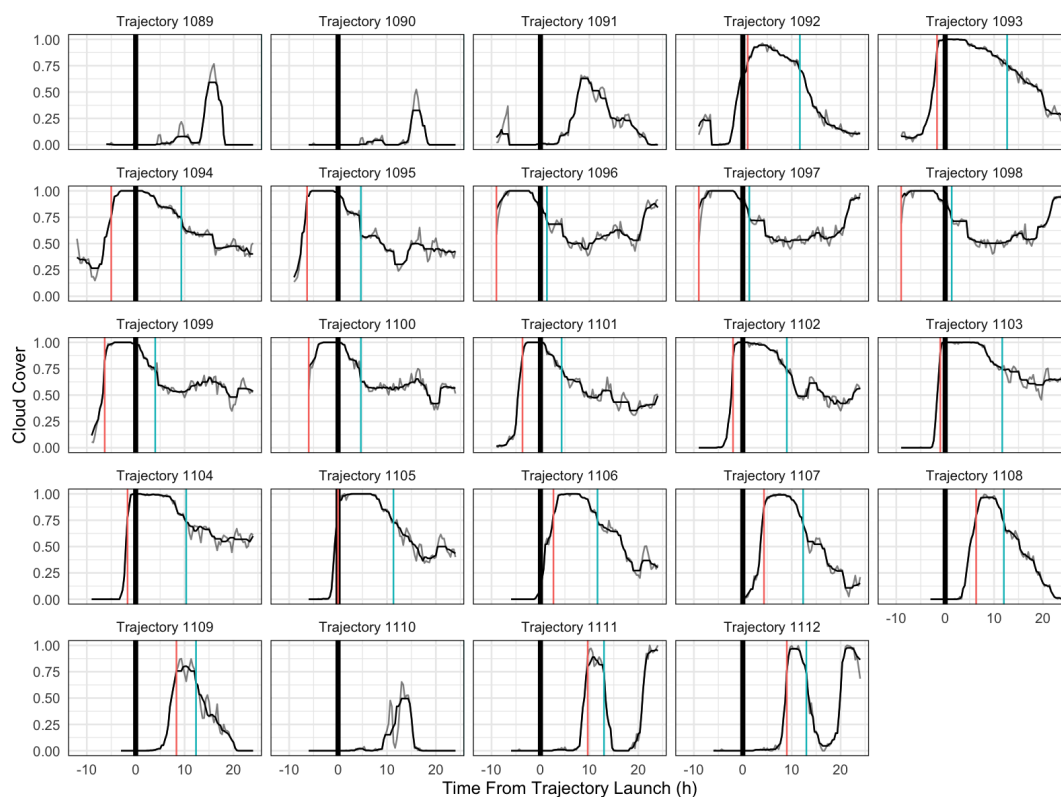


Figure A4. Timelines of cloud cover (thin gray line) along each trajectory (panel by panel) produced for the second flight on 29 March 2022 (shown in Fig. 1). A low-pass filter smooths timelines (thinner black line). The relative position to flight data (thick black vertical line) to cloud formation (red) and cloud breakup (light blue) is measured as the difference in time and downwind distance.

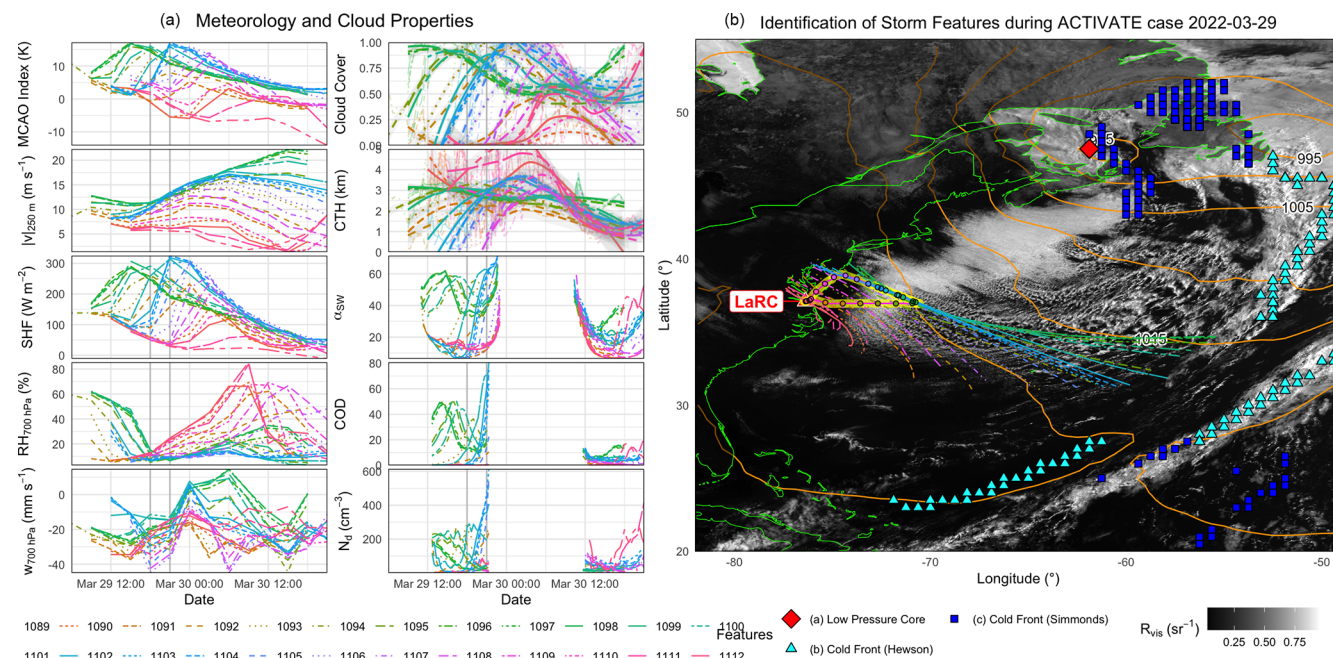


Figure A5. Various MERRA-2 meteorological and GOES-16 cloud properties (a) along all trajectories that are shown on the map (b), which is identical to Fig. 1.

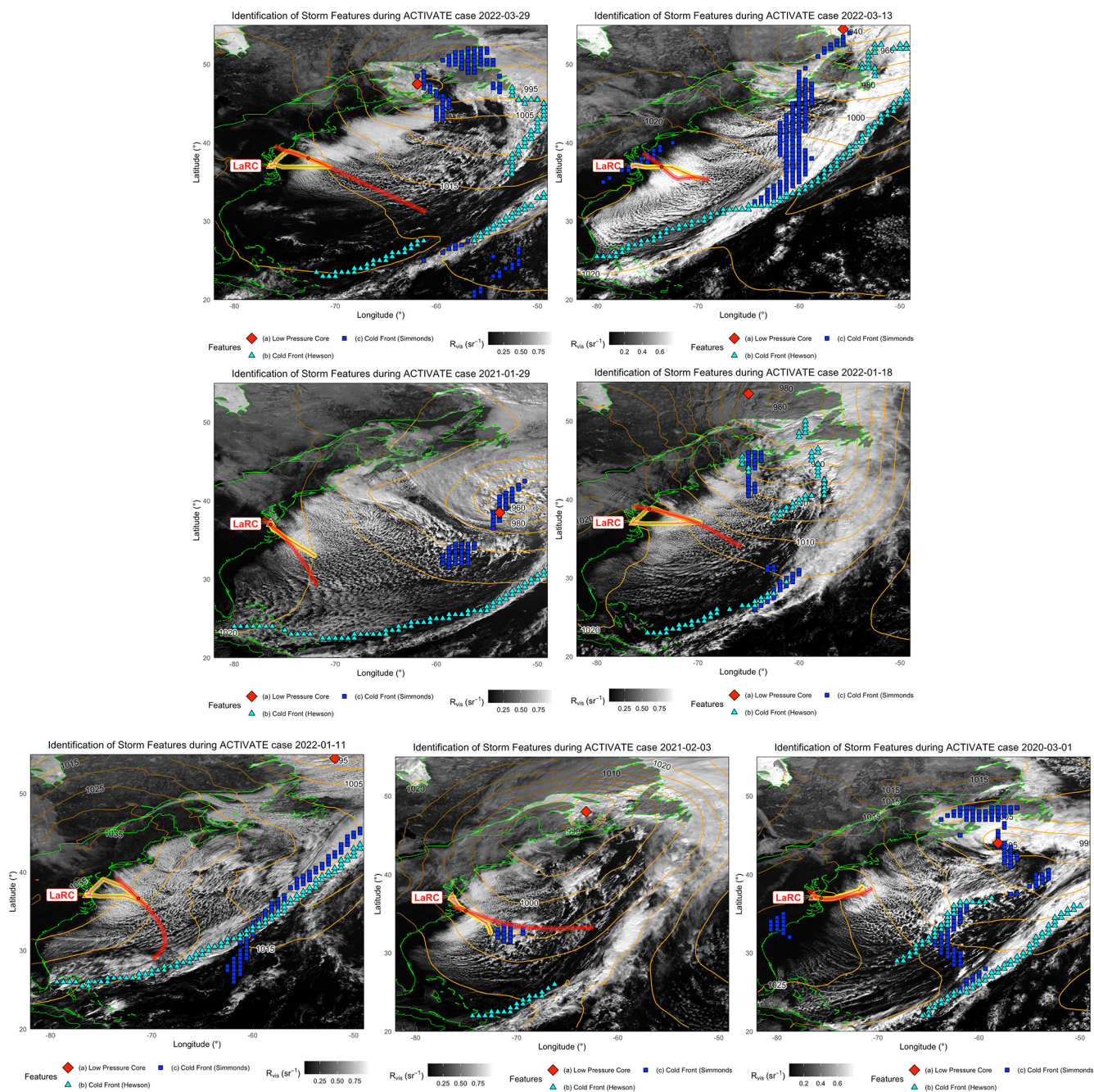


Figure A6. Similar to Fig. 1 but here shown for the first flight of each selected day (yellow) with the trajectory (red) that maximally connects both flights, determined through the maximum fraction of timestamps within 20 km and 1 h across trajectory.

Code and data availability. MERRA-2 fields (<https://doi.org/10.5067/VJAFPL1ICSIV>; Global Modeling and Assimilation Office (GMAO), 2024) were downloaded from <https://www.earthdata.nasa.gov/> (NASA/GSFC/ESPD, 2024). GOES-16 imagery was downloaded from the Space Science and Engineering Center (SSEC), University of Wisconsin–Madison, using McIDAS version 4. GOES-16 retrievals (https://doi.org/10.5067/ASDC/SUBORBITAL/ACTIVATE-Satellite_1; NASA/LaRC/SD/ASDC, 2021a) and ACTIVATE flight measurements (https://doi.org/10.5067/ASDC/ACTIVATE_Cloud_AircraftInSitu_Falcon_Data_1, NASA/LaRC/SD/ASDC, 2023, and https://doi.org/10.5067/ASDC/ACTIVATE_AerosolCloud_AircraftRemoteSensing_KingAir_Data_1, NASA/LaRC/SD/ASDC, 2021b) are publicly available via data archive at ACTIVATE's field data repository: <https://asdc.larc.nasa.gov/soot/search> (NASA/LaRC/SD/ASDC, 2019). The code to detect frontal regions using Hewson spatial gradients, is provided at <https://github.com/coecms/frontdetection/tree/main> (Green et al., 2021) and was translated into R language. Code that scores flights and summarizes cloud properties is available upon request.

Author contributions. FT carried out the analysis and prepared the manuscript. AF, AS, AA, GT, PZ, CV, SK, and BC provided feedback on the analysis and manuscript. SC and PZ provided identification of postfrontal flights. DP provided GOES-16 retrievals. CV and SK provided in situ cloud data.

Competing interests. At least one of the (co-)authors is a member of the editorial board of *Atmospheric Chemistry and Physics*. The peer-review process was guided by an independent editor, and the authors also have no other competing interests to declare.

Disclaimer. Publisher's note: Copernicus Publications remains neutral with regard to jurisdictional claims made in the text, published maps, institutional affiliations, or any other geographical representation in this paper. While Copernicus Publications makes every effort to include appropriate place names, the final responsibility lies with the authors.

Acknowledgements. This work was supported by ACTIVATE, a NASA Earth Venture Suborbital-3 (EVS-3) investigation funded by NASA's Earth Science Division and managed through the Earth System Science Pathfinder Program Office Division. The authors thank the ACTIVATE team for helpful discussion and for support with measurements and quality control. Ann Fridlind was supported by the NASA Modeling, Analysis and Prediction Program funding for ModelE development.

Financial support. ACTIVATE is a NASA Earth Venture Suborbital-3 (EVS-3) investigation funded by NASA's Earth Science Division and managed through the Earth System Science Pathfinder Program Office (grant nos. 80NSSC19K044, 80NSSC19K0442, and 80NSSC19K0390). This research was further supported by the Deutsche Forschungsgemeinschaft (grant

nos. 428312742 and 522359172) and the European Union's Horizon Europe Climate, Energy and Mobility project (grant nos. 101114785 and 101114613).

Review statement. This paper was edited by Eija Asmi and reviewed by two anonymous referees.

References

- Abel, S. J., Boutle, I. A., Waite, K., Fox, S., Brown, P. R. A., Cotton, R., Lloyd, G., Choullarton, T. W., and Bower, K. N.: The Role of Precipitation in Controlling the Transition from Stratocumulus to Cumulus Clouds in a Northern Hemisphere Cold-Air Outbreak, *J. Atmos. Sci.*, 74, 2293–2314, <https://doi.org/10.1175/JAS-D-16-0362.1>, 2017.
- Behrenfeld, M. J., Moore, R. H., Hostetler, C. A., Graff, J., Gaube, P., Russell, L. M., Chen, G., Doney, S. C., Giovannoni, S., Liu, H., Proctor, C., Bolaños, L. M., Baetge, N., Davie-Martin, C., Westberry, T. K., Bates, T. S., Bell, T. G., Bidle, K. D., Boss, E. S., Brooks, S. D., Cairns, B., Carlson, C., Halsey, K., Harvey, E. L., Hu, C., Karp-Boss, L., Kleb, M., Menden-Deuer, S., Morison, F., Quinn, P. K., Scarino, A. J., Anderson, B., Chowdhary, J., Crosbie, E., Ferrare, R., Hair, J. W., Hu, Y., Janz, S., Redemann, J., Saltzman, E., Shook, M., Siegel, D. A., Wisthaler, A., Martin, M. Y., and Ziemba, L.: The North Atlantic Aerosol and Marine Ecosystem Study (NAAMES): Science Motive and Mission Overview, *Frontiers in Marine Science*, 6, 122, <https://doi.org/10.3389/fmars.2019.00122>, 2019.
- Berry, G., Reeder, M. J., and Jakob, C.: A global climatology of atmospheric fronts, *Geophys. Res. Lett.*, 38, L04809, <https://doi.org/10.1029/2010GL046451>, 2011.
- Bock, L., Lauer, A., Schlund, M., Barreiro, M., Bellouin, N., Jones, C., Meehl, G. A., Predoi, V., Roberts, M. J., and Eyring, V.: Quantifying Progress Across Different CMIP Phases With the ESMValTool, *J. Geophys. Res.-Atmos.*, 125, e2019JD032321, <https://doi.org/10.1029/2019JD032321>, 2020.
- Bodas-Salcedo, A., Williams, K. D., Ringer, M. A., Beau, I., Cole, J. N. S., Dufresne, J.-L., Koshiro, T., Stevens, B., Wang, Z., and Yokohata, T.: Origins of the Solar Radiation Biases over the Southern Ocean in CFMIP2 Models, *J. Climate*, 27, 41–56, <https://doi.org/10.1175/JCLI-D-13-00169.1>, 2014.
- Browning, K. A.: The dry intrusion perspective of extratropical cyclone development, *Meteorolo. Appl.*, 4, 317–324, <https://doi.org/10.1017/S1350482797000613>, 1997.
- Brümmer, B.: Roll and Cell Convection in Wintertime Arctic Cold-Air Outbreaks, *J. Atmos. Sci.*, 56, 2613–2636, [https://doi.org/10.1175/1520-0469\(1999\)056<2613:RACCIW>2.0.CO;2](https://doi.org/10.1175/1520-0469(1999)056<2613:RACCIW>2.0.CO;2), 1999.
- Burton, S. P., Hostetler, C. A., Cook, A. L., Hair, J. W., Seaman, S. T., Scola, S., Harper, D. B., Smith, J. A., Fenn, M. A., Ferrare, R. A., Saide, P. E., Chemyakin, E. V., and Müller, D.: Calibration of a high spectral resolution lidar using a Michelson interferometer, with data examples from ORACLES, *Appl. Optics*, 57, 6061–6075, <https://doi.org/10.1364/AO.57.006061>, 2018.
- Cairns, B., Russell, E. E., and Travis, L. D.: Research Scanning Polarimeter: calibration and ground-based measurements, in: *Polarization: Measurement, Analysis, and Remote Sensing*

- II, edited by: Goldstein, D. H. and Chenault, D. B., International Society for Optics and Photonics, SPIE, 3754, 186–196, <https://doi.org/10.1117/12.366329>, 1999.
- Chen, J., Wang, H., Li, X., Painemal, D., Sorooshian, A., Thornhill, K. L., Robinson, C., and Shingler, T.: Impact of Meteorological Factors on the Mesoscale Morphology of Cloud Streets during a Cold-Air Outbreak over the Western North Atlantic, *J. Atmos. Sci.*, 79, 2863–2879, <https://doi.org/10.1175/JAS-D-22-0034.1>, 2022.
- Corral, A. F., Choi, Y., Crosbie, E., Dadashazar, H., DiGangi, J. P., Diskin, G. S., Fenn, M., Harper, D. B., Kirschler, S., Liu, H., Moore, R. H., Nowak, J. B., Scarino, A. J., Seaman, S., Shingler, T., Shook, M. A., Thornhill, K. L., Voigt, C., Zhang, B., Ziemba, L. D., and Sorooshian, A.: Cold Air Outbreaks Promote New Particle Formation Off the U.S. East Coast, *Geophys. Res. Lett.*, 49, e2021GL096073, <https://doi.org/10.1029/2021GL096073>, 2022.
- Dirks, R. A., Kuettner, J. P., and Moore, J. A.: Genesis of Atlantic Lows Experiment (GALE): An Overview, *B. Am. Meteorol. Soc.*, 69, 148–160, [https://doi.org/10.1175/1520-0477\(1988\)069<0148:GOALEA>2.0.CO;2](https://doi.org/10.1175/1520-0477(1988)069<0148:GOALEA>2.0.CO;2), 1988.
- Elsaesser, G. S., O'Dell, C. W., Lebsock, M. D., Bennartz, R., Greenwald, T. J., and Wentz, F. J.: The Multisensor Advanced Climatology of Liquid Water Path (MAC-LWP), *J. Climate*, 30, 10193–10210, <https://doi.org/10.1175/JCLI-D-16-0902.1>, 2017.
- Ephraim, S., Zuidema, P., Juliano, T. W., Grasmick, C., Geerts, B., French, J., Cadetdu, M., Pazmany, A., and Woods, S.: A New Neural Network Retrieval of Liquid Water Path Optimized for Mixed-Phase Cold Air Outbreaks Using Radiometer and Radar Observations, *J. Atmos. Ocean. Tech.* [preprint], <https://doi.org/10.31223/X5HQ56>, 2024.
- Field, P. R. and Wood, R.: Precipitation and Cloud Structure in Midlatitude Cyclones, *J. Climate*, 20, 233–254, <https://doi.org/10.1175/JCLI3998.1>, 2007.
- Field, P. R., Cotton, R. J., McBeath, K., Lock, A. P., Webster, S., and Allan, R. P.: Improving a convection-permitting model simulation of a cold air outbreak, *Q. J. Roy. Meteorol. Soc.*, 140, 124–138, <https://doi.org/10.1002/qj.2116>, 2014.
- Frey, W. R. and Kay, J. E.: The influence of extratropical cloud phase and amount feedbacks on climate sensitivity, *Clim. Dynam.*, 50, 3097–3116, 2018.
- Fridlind, A. M. and Ackerman, A. S.: Chapter 7 - Simulations of Arctic Mixed-Phase Boundary Layer Clouds: Advances in Understanding and Outstanding Questions, in: *Mixed-Phase Clouds*, edited by Andronache, C., Elsevier, 153–183, <https://doi.org/10.1016/B978-0-12-810549-8.00007-6>, ISBN 978-0-12-810549-8, 2018.
- Geerts, B., Giangrande, S. E., McFarquhar, G. M., Xue, L., Abel, S. J., Comstock, J. M., Crewell, S., DeMott, P. J., Ebell, K., Field, P., Hill, T. C. J., Hunzinger, A., Jensen, M. P., Johnson, K. L., Juliano, T. W., Kollias, P., Kosovic, B., Lackner, C., Luke, E., Lüpkes, C., Matthews, A. A., Neggers, R., Ovchinnikov, M., Powers, H., Shupe, M. D., Spengler, T., Swanson, B. E., Tjernström, M., Theisen, A. K., Wales, N. A., Wang, Y., Wendisch, M., and Wu, P.: The COMBLE Campaign: A Study of Marine Boundary Layer Clouds in Arctic Cold-Air Outbreaks, *B. Am. Meteorol. Soc.*, 103, E1371–E1389, <https://doi.org/10.1175/BAMS-D-21-0044.1>, 2022.
- Gelaro, R., McCarty, W., Suárez, M. J., Todling, R., Molod, A., Takacs, L., Randles, C. A., Darmenov, A., Bosilovich, M. G., Reichle, R., Wargan, K., Coy, L., Cullather, R., Draper, C., Akella, S., Buchard, V., Conaty, A., da Silva, A. M., Gu, W., Kim, G.-K., Koster, R., Lucchesi, R., Merkova, D., Nielsen, J. E., Parityka, G., Pawson, S., Putman, W., Rienecker, M., Schubert, S. D., Sienkiewicz, M., and Zhao, B.: The Modern-Era Retrospective Analysis for Research and Applications, Version 2 (MERRA-2), *J. Climate*, 30, 5419–5454, <https://doi.org/10.1175/JCLI-D-16-0758.1>, 2017.
- Global Modeling and Assimilation Office (GMAO): inst3_3d_asm_Cp: MERRA-2 3D IAU State, Meteorology Instantaneous 3-hourly (p-coord, 0.625x0.5L42), Version 5.12.4, Goddard Space Flight Center Distributed Active Archive Center (GSFC DAAC) [data set], Greenbelt, MD, USA, <https://doi.org/10.5067/VJAFPL1CSIV>, 2024.
- Green, S., Carouge, C., and Heerdegen, A.: Front Detection, GitHub [code], <https://github.com/coecms/frontdetection/tree/main> (last access: 29 April 2025), 2021.
- Hewson, T. D.: Objective fronts, *Meteorol. Appl.*, 5, 37–65, <https://doi.org/10.1017/S1350482798000553>, 1998.
- Juliano, T., Fridlind, A., Tornow, F., Williams, A., Russell, L., Sun, Y., Knopf, D., Grover, M., Collis, S., Dumas, K., and Illi, M.: COMBLE Model-Observation Intercomparison Project Cookbook, <https://github.com/ARM-Development/comble-mip> (last access: 29 April 2025), 2024.
- Kirschler, S., Voigt, C., Anderson, B., Campos Braga, R., Chen, G., Corral, A. F., Crosbie, E., Dadashazar, H., Ferrare, R. A., Hahn, V., Hendricks, J., Kaufmann, S., Moore, R., Pöhler, M. L., Robinson, C., Scarino, A. J., Schollmayer, D., Shook, M. A., Thornhill, K. L., Winstead, E., Ziemba, L. D., and Sorooshian, A.: Seasonal updraft speeds change cloud droplet number concentrations in low-level clouds over the western North Atlantic, *Atmos. Chem. Phys.*, 22, 8299–8319, <https://doi.org/10.5194/acp-22-8299-2022>, 2022.
- Kirschler, S., Voigt, C., Anderson, B. E., Chen, G., Crosbie, E. C., Ferrare, R. A., Hahn, V., Hair, J. W., Kaufmann, S., Moore, R. H., Painemal, D., Robinson, C. E., Sanchez, K. J., Scarino, A. J., Shingler, T. J., Shook, M. A., Thornhill, K. L., Winstead, E. L., Ziemba, L. D., and Sorooshian, A.: Overview and statistical analysis of boundary layer clouds and precipitation over the western North Atlantic Ocean, *Atmos. Chem. Phys.*, 23, 10731–10750, <https://doi.org/10.5194/acp-23-10731-2023>, 2023.
- Knop, I., Bansmer, S. E., Hahn, V., and Voigt, C.: Comparison of different droplet measurement techniques in the Braunschweig Icing Wind Tunnel, *Atmos. Meas. Tech.*, 14, 1761–1781, <https://doi.org/10.5194/amt-14-1761-2021>, 2021.
- Korolev, A. and Leisner, T.: Review of experimental studies of secondary ice production, *Atmos. Chem. Phys.*, 20, 11767–11797, <https://doi.org/10.5194/acp-20-11767-2020>, 2020.
- Korolev, A., Heckman, I., Wolde, M., Ackerman, A. S., Fridlind, A. M., Ladino, L. A., Lawson, R. P., Milbrandt, J., and Williams, E.: A new look at the environmental conditions favorable to secondary ice production, *Atmos. Chem. Phys.*, 20, 1391–1429, <https://doi.org/10.5194/acp-20-1391-2020>, 2020.
- Lawson, R. P., O'Connor, D., Zmarzly, P., Weaver, K., Baker, B., Mo, Q., and Jonsson, H.: The 2D-S (Stereo) Probe: Design and Preliminary Tests of a New Airborne, High-Speed, High-Resolution Particle Imaging Probe, *J. Atmos. Ocean. Tech.*, 23, 1462–1477, <https://doi.org/10.1175/JTECH1927.1>, 2006.

- Li, X.-Y., Wang, H., Chen, J., Endo, S., George, G., Cairns, B., Chellappan, S., Zeng, X., Kirschler, S., Voigt, C., Sorooshian, A., Crosbie, E., Chen, G., Ferrare, R. A., Gustafson, W. I., Hair, J. W., Kleb, M. M., Liu, H., Moore, R., Painemal, D., Robinson, C., Scarino, A. J., Shook, M., Shingler, T. J., Thornhill, K. L., Tornow, F., Xiao, H., Ziemba, L. D., and Zuidema, P.: Large-eddy simulations of marine boundary-layer clouds associated with cold air outbreaks during the ACTIVATE campaign – Part I: Case setup and sensitivities to large-scale forcings, *J. Atmos. Sci.*, 79, 73–100, <https://doi.org/10.1175/JAS-D-21-0123.1>, 2021.
- McCoy, D. T., Field, P. R., Elsaesser, G. S., Bodas-Salcedo, A., Kahn, B. H., Zelinka, M. D., Kodama, C., Mauritsen, T., Vanniere, B., Roberts, M., Vidale, P. L., Saint-Martin, D., Voldoire, A., Haarsma, R., Hill, A., Shipway, B., and Wilkinson, J.: Cloud feedbacks in extratropical cyclones: insight from long-term satellite data and high-resolution global simulations, *Atmos. Chem. Phys.*, 19, 1147–1172, <https://doi.org/10.5194/acp-19-1147-2019>, 2019.
- McCoy, D. T., Frazer, M. E., Mülmenstädt, J., Tan, I., Terai, C. R., and Zelinka, M. D.: Extratropical Cloud Feedbacks, American Geophysical Union (AGU), Chap. 6, 133–157, <https://doi.org/10.1002/9781119700357.ch6>, ISBN 9781119700357, 2023.
- McCoy, I. L., Wood, R., and Fletcher, J. K.: Identifying Meteorological Controls on Open and Closed Mesoscale Cellular Convection Associated with Marine Cold Air Outbreaks, *J. Geophys. Res.-Atmos.*, 122, 11678–11702, <https://doi.org/10.1002/2017JD027031>, 2017.
- Mech, M., Ehrlich, A., Herber, A., Lüpkes, C., Wendisch, M., Becker, S., Boose, Y., Chechin, D., Crewell, S., Dupuy, R., Gourbeyre, C., Hartmann, J., Jäkel, E., Jourdan, O., Kliesch, L.-L., Klingebiel, M., Kulla, B. S., Mioche, G., Moser, M., Risse, N., Ruiz-Donoso, E., Schäfer, M., Stapf, J., and Voigt, C.: MOSAiC-ACA and AFLUX-Arctic airborne campaigns characterizing the exit area of MOSAiC, *Scientific Data*, 9, 790, <https://doi.org/10.1038/s41597-022-01900-7>, 2022.
- Minnis, P. and Heck, P.: GOES-R Advanced Baseline Imager (ABI) Algorithm Theoretical Basis Document for Night-time Cloud Optical Depth, Cloud Particle Size, Cloud Ice Water Path, and Cloud Liquid Water Path, NOAA NESDIS, Center for Satellite Applications and Research, https://www.star.nesdis.noaa.gov/goesr/documents/ATBDs/Baseline/ATBD_GOES-R_Cloud_NCOMP_v3.0_Jul2012.pdf (last access: 29 April 2025), 2012.
- Moser, M., Voigt, C., Jurkat-Witschas, T., Hahn, V., Mioche, G., Jourdan, O., Dupuy, R., Gourbeyre, C., Schwarzenboeck, A., Lucke, J., Boose, Y., Mech, M., Borrmann, S., Ehrlich, A., Herber, A., Lüpkes, C., and Wendisch, M.: Microphysical and thermodynamic phase analyses of Arctic low-level clouds measured above the sea ice and the open ocean in spring and summer, *Atmos. Chem. Phys.*, 23, 7257–7280, <https://doi.org/10.5194/acp-23-7257-2023>, 2023.
- Namdari, S., Ajayi, T., Choi, Y., Crosbie, E. C., DiGangi, J. P., Diskin, G. S., Kirschler, S., Liu, H., Nowak, J. B., Shook, M. A., Soloff, C., Thornhill, K. L., Voigt, C., Winstead, E. L., Zhang, B., Ziemba, L. D., and Sorooshian, A.: A comprehensive analysis of new particle formation across the northwest Atlantic: Analysis of ACTIVATE airborne data, *Atmos. Environ.*, 338, 120831, <https://doi.org/10.1016/j.atmosenv.2024.120831>, 2024.
- NASA/GSFC/ESPD: Earthdata Search, Earth Science Data and Information System (ESDIS) Project, Earth Science Projects Division (ESPD), Flight Projects Directorate, Goddard Space Flight Center (GSFC) National Aeronautics and Space Administration (NASA), Greenbelt, MD, <https://www.earthdata.nasa.gov/> (last access: 6 March 2025), 2024.
- NASA/LARC/SD/ASDC: Sub-Orbital Order Tool (SOOT), NASA Langley Atmospheric Science Data Center DAAC, <https://asdc.larc.nasa.gov/soot/search> (last access: 6 March 2025), 2019.
- NASA/LARC/SD/ASDC: ACTIVATE GOES-16 Supplementary Data Products, NASA Langley Atmospheric Science Data Center DAAC [data set], https://doi.org/10.5067/ASDC/SUBORBITAL/ACTIVATE-Satellite_1, 2021a.
- NASA/LARC/SD/ASDC: ACTIVATE King Air Aerosol and Cloud Remotely Sensed Data, NASA Langley Atmospheric Science Data Center DAAC [data set], https://doi.org/10.5067/ASDC/ACTIVATE_AerosolCloud_AircraftRemoteSensing_KingAir_Data_1, 2021b.
- NASA/LARC/SD/ASDC: ACTIVATE Falcon In Situ Cloud Data, NASA Langley Atmospheric Science Data Center DAAC [data set], https://doi.org/10.5067/ASDC/ACTIVATE_Cloud_AircraftInSitu_Falcon_Data_1, 2023.
- Naud, C. M., Booth, J. F., and Genio, A. D. D.: The Relationship between Boundary Layer Stability and Cloud Cover in the Post-Cold-Frontal Region, *J. Climate*, 29, 8129–8149, <https://doi.org/10.1175/JCLI-D-15-0700.1>, 2016.
- Neggers, R. A. J.: Attributing the behavior of low-level clouds in large-scale models to subgrid-scale parameterizations, *J. Adv. Model. Earth Sy.*, 7, 2029–2043, <https://doi.org/10.1002/2015MS000503>, 2015.
- Painemal, D., Chellappan, S., Smith Jr., W. L., Spangenberg, D., Park, J. M., Ackerman, A., Chen, J., Crosbie, E., Ferrare, R., Hair, J., Kirschler, S., Li, X.-Y., McComiskey, A., Moore, R. H., Sanchez, K., Sorooshian, A., Tornow, F., Voigt, C., Wang, H., Winstead, E., Zeng, X., Ziemba, L., and Zuidema, P.: Wintertime Synoptic Patterns of Midlatitude Boundary Layer Clouds Over the Western North Atlantic: Climatology and Insights From In Situ ACTIVATE Observations, *J. Geophys. Res.-Atmos.*, 128, e2022JD037725, <https://doi.org/10.1029/2022JD037725>, 2023.
- Pithan, F., Svensson, G., Caballero, R., Chechin, D., Cronin, T. W., Ekman, A. M. L., Neggers, R., Shupe, M. D., Solomon, A., Tjernström, M., and Wendisch, M.: Role of air-mass transformations in exchange between the Arctic and mid-latitudes, *Nat. Geosci.*, 11, 805–812, <https://doi.org/10.1038/s41561-018-0234-1>, 2019.
- Raveh-Rubin, S.: Dry Intrusions: Lagrangian Climatology and Dynamical Impact on the Planetary Boundary Layer, *J. Climate*, 30, 6661–6682, <https://doi.org/10.1175/JCLI-D-16-0782.1>, 2017.
- Sanchez, K. J., Chen, C.-L., Russell, L. M., Betha, R., Liu, J., Price, D. J., Massoli, P., Ziemba, L. D., Crosbie, E. C., Moore, R. H., Müller, M., Schiller, S. A., Wisthaler, A., Lee, A. K. Y., Quinn, P. K., Bates, T. S., Porter, J., Bell, T. G., Saltzman, E. S., Vaillancourt, R. D., and Behrenfeld, M. J.: Substantial seasonal contribution of observed biogenic sulfate particles to cloud condensation nuclei, *Scientific Reports*, 8, 3235, <https://doi.org/10.1038/s41598-018-21590-9>, 2018.

- Schlosser, J. S., Bennett, R., Cairns, B., Chen, G., Collister, B. L., Hair, J. W., Jones, M., Shook, M. A., Sorooshian, A., Thornhill, K. L., Ziemba, L. D., and Stammes, S.: Maximizing the Volume of Collocated Data from Two Coordinated Suborbital Platforms, *J. Atmos. Ocean. Tech.*, 41, 189–201, <https://doi.org/10.1175/JTECH-D-23-0001.1>, 2024.
- Seethala, C., Zuidema, P., Edson, J., Brunke, M., Chen, G., Li, X.-Y., Painemal, D., Robinson, C., Shingler, T., Shook, M., Sorooshian, A., Thornhill, L., Tornow, F., Wang, H., Zeng, X., and Ziemba, L.: On Assessing ERA5 and MERRA2 Representations of Cold-Air Outbreaks Across the Gulf Stream, *Geophys. Res. Lett.*, 48, e2021GL094364, <https://doi.org/10.1029/2021GL094364>, 2021.
- Seethala, C., Zuidema, P., Kirschler, S., Voigt, C., Cairns, B., Crosbie, E. C., Ferrare, R., Hair, J., Painemal, D., Shingler, T., Shook, M., Thornhill, K. L., Tornow, F., and Sorooshian, A.: Microphysical Evolution in Mixed-Phase Midlatitude Marine Cold-Air Outbreaks, *J. Atmos. Sci.*, 81, 1725–1747, 2024.
- Seidel, J. S., Kiselev, A. A., Keinert, A., Stratmann, F., Leisner, T., and Hartmann, S.: Secondary ice production – no evidence of efficient rime-splintering mechanism, *Atmos. Chem. Phys.*, 24, 5247–5263, <https://doi.org/10.5194/acp-24-5247-2024>, 2024.
- Simmonds, I., Keay, K., and Bye, J. A. T.: Identification and Climatology of Southern Hemisphere Mobile Fronts in a Modern Reanalysis, *J. Climate*, 25, 1945–1962, <https://doi.org/10.1175/JCLI-D-11-00100.1>, 2012.
- Sorooshian, A., Anderson, B., Bauer, S. E., Braun, R. A., Cairns, B., Crosbie, E., Dadashazar, H., Diskin, G., Ferrare, R., Flagan, R. C., Hair, J., Hostetler, C., Jonsson, H. H., Kleb, M. M., Liu, H., MacDonald, A. B., McComiskey, A., Moore, R., Painemal, D., Russell, L. M., Seinfeld, J. H., Shook, M., Smith, W. L., Thornhill, K., Tselioudis, G., Wang, H., Zeng, X., Zhang, B., Ziemba, L., and Zuidema, P.: Aerosol–cloud–meteorology interaction airborne field investigations: Using lessons learned from the US West Coast in the design of ACTIVATE off the US East Coast, *B. Am. Meteorol. Soc.*, 100, 1511–1528, 2019.
- Sorooshian, A., Corral, A. F., Braun, R. A., Cairns, B., Crosbie, E., Ferrare, R., Hair, J., Kleb, M. M., Hossein Mardi, A., Maring, H., McComiskey, A., Moore, R., Painemal, D., Scarino, A. J., Schlosser, J., Shingler, T., Shook, M., Wang, H., Zeng, X., Ziemba, L., and Zuidema, P.: Atmospheric Research Over the Western North Atlantic Ocean Region and North American East Coast: A Review of Past Work and Challenges Ahead, *J. Geophys. Res.-Atmos.*, 125, e2019JD031626, <https://doi.org/10.1029/2019JD031626>, 2020.
- Sorooshian, A., Alexandrov, M. D., Bell, A. D., Bennett, R., Betito, G., Burton, S. P., Buzanowicz, M. E., Cairns, B., Chemyakin, E. V., Chen, G., Choi, Y., Collister, B. L., Cook, A. L., Corral, A. F., Crosbie, E. C., van Diedenhoven, B., DiGangi, J. P., Diskin, G. S., Dmitrovic, S., Edwards, E.-L., Fenn, M. A., Ferrare, R. A., van Gilst, D., Hair, J. W., Harper, D. B., Hilario, M. R. A., Hostetler, C. A., Jester, N., Jones, M., Kirschler, S., Kleb, M. M., Kusterer, J. M., Leavor, S., Lee, J. W., Liu, H., McCauley, K., Moore, R. H., Nied, J., Notari, A., Nowak, J. B., Painemal, D., Phillips, K. E., Robinson, C. E., Scarino, A. J., Schlosser, J. S., Seaman, S. T., Seethala, C., Shingler, T. J., Shook, M. A., Sinclair, K. A., Smith Jr., W. L., Spangenberg, D. A., Stammes, S. A., Thornhill, K. L., Voigt, C., Vömel, H., Wasilewski, A. P., Wang, H., Winstead, E. L., Zeider, K., Zeng, X., Zhang, B., Ziemba, L. D., and Zuidema, P.: Spatially coordinated airborne data and complementary products for aerosol, gas, cloud, and meteorological studies: the NASA ACTIVATE dataset, *Earth Syst. Sci. Data*, 15, 3419–3472, <https://doi.org/10.5194/essd-15-3419-2023>, 2023.
- Tomassini, L., Field, P. R., Honnert, R., Malardel, S., McTaggart-Cowan, R., Saitou, K., Noda, A. T., and Seifert, A.: The “Grey Zone” cold air outbreak global model intercomparison: A cross evaluation using large-eddy simulations, *J. Adv. Model. Earth Sy.*, 9, 39–64, <https://doi.org/10.1002/2016MS000822>, 2017.
- Tornow, F., Ackerman, A. S., and Fridlind, A. M.: Preconditioning of overcast-to-broken cloud transitions by riming in marine cold air outbreaks, *Atmos. Chem. Phys.*, 21, 12049–12067, <https://doi.org/10.5194/acp-21-12049-2021>, 2021.
- Tornow, F., Ackerman, A. S., Fridlind, A. M., Cairns, B., Crosbie, E. C., Kirschler, S., Moore, R. H., Painemal, D., Robinson, C. E., Seethala, C., Shook, M. A., Voigt, C., Winstead, E. L., Ziemba, L. D., Zuidema, P., and Sorooshian, A.: Dilution of Boundary Layer Cloud Condensation Nucleus Concentrations by Free Tropospheric Entrainment During Marine Cold Air Outbreaks, *Geophys. Res. Lett.*, 49, e2022GL098444, <https://doi.org/10.1029/2022GL098444>, 2022.
- Tornow, F., Ackerman, A. S., Fridlind, A. M., Tselioudis, G., Cairns, B., Painemal, D., and Elsaesser, G.: On the impact of a dry intrusion driving cloud-regime transitions in a midlatitude cold-air outbreak, *J. Atmos. Sci.*, 80, 2881–2896, 2023.
- Tornow, F., Crosbie, E., Fridlind, A., et al.: High accumulation mode aerosol concentration and low aerosol hygroscopicity limit impacts of recent particle formation on Northwest Atlantic post-frontal clouds, *ESS Open Archive*, <https://doi.org/10.22541/essoar.174319801.18907793/v1>, 2025.
- Tselioudis, G. and Grise, K.: Midlatitude cloud systems, in: *Clouds and Climate: Climate Science's Greatest Challenge*, edited by: Siebesma, A. P., Bony, S., Jakob, C., and Stevens, B., Cambridge University Press, 279–296, ISBN: 9781107061071, 1107061075, 2020.
- Wang, J., Wood, R., Jensen, M., Azevedo, E., Bretherton, C., Chand, D., Chiu, C., Dong, X., Fast, J., Gettleman, A., Ghan, S., Giannandrea, S., Gilles, M., Jefferson, A., Kollias, P., Kuang, C., Laskin, A., Lewis, E., Liu, X., Liu, Y., Luke, E., McComiskey, A., Mei, F., Miller, M., Sedlacek, A., and Shaw, R.: Aerosol and Cloud Experiments in Eastern North Atlantic (ACE-ENA) Field Campaign Report, Tech. rep., DOE Office of Science Atmospheric Radiation Measurement (ARM) Program, Report Number: DOE/SC-ARM-19-012, OSTI ID: 1526025, <https://www.osti.gov/biblio/1526025> (last access: 29 April 2025), 2019.
- Wendisch, M., Brückner, M., Crewell, S., et al.: Atmospheric and surface processes, and feedback mechanisms determining Arctic amplification: A review of first results and prospects of the (AC)³ project, *B. Am. Meteorol. Soc.*, 104, E208–E242, 2023.
- Wendisch, M., Crewell, S., Ehrlich, A., Herber, A., Kirbus, B., Lüpkes, C., Mech, M., Abel, S. J., Akansu, E. F., Ament, F., Aubry, C., Becker, S., Borrmann, S., Bozem, H., Brückner, M., Clemen, H.-C., Dahlke, S., Dekoutsidis, G., Delanoë, J., De La Torre Castro, E., Dorff, H., Dupuy, R., Eppers, O., Ewald, F., George, G., Gorodetskaya, I. V., Grawe, S., Groß, S., Hartmann, J., Henning, S., Hirsch, L., Jäkel, E., Joppe, P., Jourdan, O., Jurányi, Z., Karalis, M., Kellermann, M., Klingebiel, M., Lonardi, M., Lucke, J., Luebke, A. E., Maahn, M., Mahernndl, N., Maturilli, M., Mayer,

- B., Mayer, J., Mertes, S., Michaelis, J., Michalkov, M., Mioche, G., Moser, M., Müller, H., Neggers, R., Ori, D., Paul, D., Paulus, F. M., Pilz, C., Pithan, F., Pöhlker, M., Pörtge, V., Ringel, M., Risse, N., Roberts, G. C., Rosenburg, S., Röttenbacher, J., Rückert, J., Schäfer, M., Schaefer, J., Schemann, V., Schirmacher, I., Schmidt, J., Schmidt, S., Schneider, J., Schnitt, S., Schwarz, A., Siebert, H., Sodemann, H., Sperzel, T., Spreen, G., Stevens, B., Stratmann, F., Svensson, G., Tatzelt, C., Tuch, T., Vihma, T., Voigt, C., Volkmer, L., Walbröl, A., Weber, A., Wehner, B., Wetzel, B., Wirth, M., and Zinner, T.: Overview: quasi-Lagrangian observations of Arctic air mass transformations – introduction and initial results of the HALO-(AC)³ aircraft campaign, *Atmos. Chem. Phys.*, 24, 8865–8892, <https://doi.org/10.5194/acp-24-8865-2024>, 2024.
- Williams, A. S., Dedrick, J. L., Russell, L. M., Tornow, F., Silber, I., Fridlind, A. M., Swanson, B., DeMott, P. J., Zieger, P., and Krejci, R.: Aerosol size distribution properties associated with cold-air outbreaks in the Norwegian Arctic, *Atmos. Chem. Phys.*, 24, 11791–11805, <https://doi.org/10.5194/acp-24-11791-2024>, 2024.
- Wood, R., Stemmler, J. D., Rémillard, J., and Jefferson, A.: Low-CCN concentration air masses over the eastern North Atlantic: Seasonality, meteorology, and drivers, *J. Geophys. Res.-Atmos.*, 122, 1203–1223, <https://doi.org/10.1002/2016JD025557>, 2017.
- Wyant, M. C., Bretherton, C. S., Rand, H. A., and Stevens, D. E.: Numerical Simulations and a Conceptual Model of the Stratocumulus to Trade Cumulus Transition, *J. Atmos. Sci.*, 54, 168–192, [https://doi.org/10.1175/1520-0469\(1997\)054<0168:NSAACM>2.0.CO;2](https://doi.org/10.1175/1520-0469(1997)054<0168:NSAACM>2.0.CO;2), 1997.
- Yamaguchi, T., Feingold, G., and Kazil, J.: Stratocumulus to Cumulus Transition by Drizzle, *J. Adv. Model. Earth Sy.*, 9, 2333–2349, <https://doi.org/10.1002/2017MS001104>, 2017.
- Zelinka, M. D., Myers, T. A., McCoy, D. T., Po-Chedley, S., Caldwell, P. M., Ceppi, P., Klein, S. A., and Taylor, K. E.: Causes of Higher Climate Sensitivity in CMIP6 Models, *Geophys. Res. Lett.*, 47, e2019GL085782, <https://doi.org/10.1029/2019GL085782>, 2020.
- Zelinka, M. D., Klein, S. A., Qin, Y., and Myers, T. A.: Evaluating climate models' cloud feedbacks against expert judgment, *J. Geophys. Res.-Atmos.*, 127, e2021JD035198, <https://doi.org/10.1029/2021JD035198>, 2022.
- Zheng, G., Wang, Y., Wood, R., Jensen, M. P., Kuang, C., McCoy, I. L., Matthews, A., Mei, F., Tomlinson, J. M., Shilling, J. E., Zawadowicz, M. A., Crosbie, E., Moore, R., Ziemba, L., Andreae, M. O., and Wang, J.: New particle formation in the remote marine boundary layer, *Nat. Commun.*, 12, 527, <https://doi.org/10.1038/s41467-020-20773-1>, 2021.